

Uncovering Non-Fermi-Liquid Behavior in Hund Metals: Conformal Field Theory Analysis of an $SU(2) \times SU(3)$ Spin-Orbital Kondo Model

E. Walter,¹ K. M. Stadler,¹ S.-S. B. Lee,¹ Y. Wang,² G. Kotliar,^{2,3} A. Weichselbaum,^{2,1} and J. von Delft¹

¹*Arnold Sommerfeld Center for Theoretical Physics, Center for NanoScience, and Munich Center for Quantum Science and Technology, Ludwig-Maximilians-Universität München, 80333 Munich, Germany*

²*Condensed Matter Physics and Materials Science Department,
Brookhaven National Laboratory, Upton, New York 11973, USA*

³*Department of Physics and Astronomy, Rutgers University, Piscataway, New Jersey 08854, USA*

(Dated: October 18, 2021)

Hund metals have attracted attention in recent years due to their unconventional superconductivity, which supposedly originates from non-Fermi-liquid (NFL) properties of the normal state. When studying Hund metals using dynamical mean-field theory, one arrives at a self-consistent “Hund impurity problem” involving a multiorbital quantum impurity with nonzero Hund coupling interacting with a metallic bath. If its spin and orbital degrees of freedom are screened at different energy scales, $T_{\text{sp}} < T_{\text{orb}}$, the intermediate energy window is governed by a novel NFL fixed point, whose nature had not yet been clarified. We resolve this problem by providing an analytical solution of a paradigmatic example of a Hund impurity problem, involving two spin and three orbital degrees of freedom. To this end, we combine a state-of-the-art implementation of the numerical renormalization group, capable of exploiting non-Abelian symmetries, with a generalization of Affleck and Ludwig’s conformal field theory (CFT) approach for multichannel Kondo models. We characterize the NFL fixed point of Hund metals in detail for a Kondo model with an impurity forming an $SU(2) \times SU(3)$ spin-orbital multiplet, tuned such that the NFL energy window is very wide. The impurity’s spin and orbital susceptibilities then exhibit striking power-law behavior, which we explain using CFT arguments. We find excellent agreement between CFT predictions and numerical renormalization group results. Our main physical conclusion is that the regime of spin-orbital separation, where orbital degrees of freedom have been screened but spin degrees of freedom have not, features anomalously strong local spin fluctuations: the impurity susceptibility increases as $\chi_{\text{sp}}^{\text{imp}} \sim \omega^{-\gamma}$, with $\gamma > 1$.

I. INTRODUCTION

A. Motivation: Hund metals

Hund metals are multiorbital materials with broad bands which are correlated via the ferromagnetic Hund coupling J_{H} , rather than the Hubbard interaction U . The coupling J_{H} implements Hund’s rule, favoring electronic states with maximal spin, which causes Hund metals to be fundamentally different from Mott insulators. This is a new exciting area of condensed matter physics; for a recent review with numerous references, see Ref. [1]. Hund metals are a very diverse class of materials, including transition metal oxides with partially filled d shells, such as the iron-based pnictide and selenide superconductors, the ruthenates, and many others [1–13].

The iron-based superconductors, in particular, raised much interest in recent years because of the unconventional nature of their superconductivity. It has been argued that the Hund nature of their normal state is essential for the onset of superconductivity [14]. In particular, spin fluctuations with a power-law divergent susceptibility $\propto \omega^{-\gamma}$, with $\gamma > 1$, have been evoked in an explanation for the anomalously large ratio of $2\Delta_{\text{max}}/T_{\text{c}}$ observed experimentally, where Δ_{max} is the maximum superconducting gap and T_{c} the critical temperature [14]. The normal state of Hund metals is of great interest on its own, since it typically shows bad-metal behavior [6, 15, 16]. Motivated by these considerations,

computational and experimental studies of Hund metals have begun to uncover their rich physics in recent years [4, 5, 8, 11, 12, 17–21].

When studying Hund metals in the context of dynamical mean-field theory (DMFT), the problem of a crystal lattice with many strongly interacting lattice sites is mapped onto a “Hund impurity,” coupled self-consistently to an effective noninteracting metallic bath. A Hund impurity has both spin *and* orbital degrees of freedom and a finite Hund coupling, favoring a large local spin.

A particularly fascinating consequence of the interplay between spin and orbital degrees of freedom is the phenomenon of spin-orbital separation (SOS): Kondo screening of Hund impurity models occurs in two stages, and the energy scales below which free spin and orbital degrees are screened differ, $T_{\text{sp}} < T_{\text{orb}}$ [8, 9, 22–24]. The low-energy regime below T_{sp} shows Fermi-liquid (FL) behavior. The intermediate SOS window $[T_{\text{sp}}, T_{\text{orb}}]$, by contrast, shows incoherent behavior, featuring almost fully screened orbital degrees of freedom coupled to almost free spin degrees of freedom. The incoherent regime has been conjectured to have non-Fermi-liquid (NFL) properties and argued to be relevant for the bad-metal behavior of Hund metals [8, 25]. However, the nature of the putative underlying NFL state has not yet been clarified.

A major obstacle for analyzing the conjectured NFL regime of Hund metals has been a lack of detailed, analytical understanding of the basic properties of Hund

impurity models, since theoretical work has overwhelmingly focused on Kondo models without orbital degrees of freedom. In this work, we overcome this obstacle in the context of an instructive case study of a specific Hund impurity model.

Before specifying the latter in detail, though, let us put our study into perspective by providing a brief historical overview of Hund impurity models.

B. Brief history of Hund impurity models

Hund impurity models are natural multiorbital generalizations of single-orbital magnetic impurity models such as the Kondo model used by Kondo in 1964 to explain the resistance minimum in magnetic alloys [26]. The search for a detailed understanding of the Kondo model beyond Kondo's perturbative calculation was a cornerstone toward the development of renormalization group techniques, starting with Anderson's poor man's scaling approach [27] and culminating in Wilson's numerical renormalization group (NRG) [28]. These methods confirmed that below a characteristic Kondo temperature the metallic bath screens the impurity spin, leading to the formation of a singlet state between impurity and conduction electrons.

Following these findings, naturally the question arises: What happens if the impurity has multiple orbitals? In particular, electrons on a multiorbital impurity experience not only a Coulomb interaction stabilizing a magnetic moment on the impurity, but also a Hund coupling, enforcing the effect of Hund's rule to maximize the total impurity spin. These two interactions lead to an intricate interplay, crucially depending on the number of electrons on the impurity. Indeed, it had been observed already in the 1960s that the Kondo scale for impurities in transition metal alloys with partially filled *d*shells decreases exponentially as the shell filling approaches 1/2 [29, 30], drawing attention to the question of understanding Kondo screening in the presence of multiple orbitals. Coqblin and Schrieffer [31] developed a generalization of the Kondo model for multiorbital impurities, yet only involving the spin degree of freedom. Okada and Yosida [32] included orbital degrees of freedom and in particular pointed out the importance of a finite Hund coupling, enforcing the effect of Hund's rule in such multiorbital systems. However, theoretical tools for analyzing a model with non-zero Hund coupling away from half filling were lacking at the time.

Later, Nozières and Blandin [33] studied a spin Kondo impurity immersed in a metallic bath with multiple orbital channels. A major conclusion of their work was that such models lead to overscreening of the impurity spin and NFL behavior, if the number of channels exceeds twice the impurity spin ($k > 2S$). This generated great theoretical interest in multichannel Kondo models, including exact Bethe solutions providing information on thermodynamical properties [34–39], and NRG

studies [40, 41]. Affleck and Ludwig (AL) [42–46] developed a powerful conformal field theory (CFT) approach for studying the strong-coupling fixed points of such multiband Kondo models, providing analytical results for finite-size spectra and the scaling behavior of correlation functions. However, their work was restricted to pure spin impurities without nontrivial orbital structure. Thus, their methods have not yet been applied to Hund impurity models, including orbital degrees of freedom and a finite Hund coupling.

In this work, we fill this long-standing void and provide a detailed and comprehensive analysis of a prototypical Hund impurity model (specified below). We achieve this by advancing and combining two powerful complementary techniques that both arose in the very context of Kondo physics: An *analytical* solution based on AL's celebrated CFT approach, generalized from a pure spin impurity to one with spin and orbital structure, and a quasiexact *numerical* solution using a state-of-the-art implementation of Wilson's NRG, allowing studies of multiorbital systems by fully exploiting Abelian and non-Abelian symmetries. This allows us to achieve a detailed understanding of the NFL behavior arising in this Hund impurity model.

C. Minimal models for Hund metals

We next describe the considerations motivating the specific choice of model studied below.

A minimal model for Hund metals has been proposed in Ref. [8]. It is a three-orbital Hubbard-Hund model, and it has been studied extensively in Refs. [2, 6, 9, 11, 22–24, 47]. A treatment of this model by DMFT at 1/3 filling yields a self-consistent Hund impurity model. More specifically, one obtains a self-consistent three-orbital Anderson-Hund (3oAH) model, in which bath and impurity both have spin *and* orbital degrees of freedom. The impurity hosts two electrons forming an antisymmetric orbital triplet and a symmetric spin triplet ($S = 1$), reflecting Hund's rule. At energies so low that charge fluctuations can be treated by a Schrieffer-Wolff transformation [9], the 3oAH model maps onto a three-channel spin-orbital Kondo (3soK) model whose impurity forms a (3×3) -dimensional $SU(2) \times SU(3)$ spin-orbital multiplet.

The 3oAH model exhibits SOS [8, 9, 22–24]. Within the SOS window $[T_{sp}, T_{orb}]$, the imaginary part of the spin susceptibility scales as $\chi_{sp}^{imp} \sim \omega^{-6/5}$ [22, 47]. The fact that the exponent, $\gamma = 6/5$, is larger than 1 has been argued to lead to the anomalous superconducting state of the iron pnictide Hund metals, as mentioned above [14]. However, the origin of this power law has remained unclear. One impediment toward finding an explanation is the fact that for the 3oAH model the orbital and spin screening scales cannot be tuned independently. The SOS window turns out to be rather small, masking the NFL behavior expected to occur within it.

In this paper, we sidestep this limitation by instead

studying the 3soK model and treating its exchange couplings as independent parameters, freed from the shackles of their 3oAH origin. We tune these such that the regime of SOS is very wide, with $T_{\text{sp}} \ll T_{\text{orb}}$. This enables us to characterize the NFL fixed point obtained for $T_{\text{sp}} = 0$, which also governs the intermediate NFL window if $T_{\text{sp}} \ll T_{\text{orb}}$. We compute fixed-point spectra and the scaling behavior of dynamical spin and orbital susceptibilities using both NRG and CFT, with mutually consistent results. In particular, we find an analytical explanation for the peculiar power law $\chi_{\text{sp}}^{\text{imp}} \sim \omega^{-6/5}$. It turns out to be governed (albeit somewhat indirectly) by the NFL fixed point mentioned above. Finally, we demonstrate the relevance of these 3soK results for the low-energy behavior of the 3oAH model by employing a hybrid Anderson-Kondo model which smoothly interpolates between the physics of the 3soK and 3oAH models. This interpolation shows that our new results also shed light on previous DMFT results for a self-consistent 3oAH model [22, 47].

Our CFT analysis builds on that devised by AL [42–46] for the k -channel Kondo model, describing k spinful channels exchange coupled to an impurity with spin S , but no orbital degrees of freedom. If $k > 2S$, the impurity spin is overscreened. AL described the corresponding NFL fixed point using a charge-spin-orbital $U(1) \times SU(2)_k \times SU(k)_2$ Kac-Moody (KM) decomposition of the bath states, and fusing the spin degrees of freedom of impurity and bath using $SU(2)_k$ fusion rules. Here we generalize this strategy to our situation, where the impurity has spin *and* orbital “isospin” degrees of freedom: the NFL fixed point at $T_{\text{sp}} = 0$ can be understood by applying $SU(3)_2$ fusion rules in the orbital sector, leading to orbital overscreening. If T_{sp} is nonzero (but $\ll T_{\text{orb}}$), the overscreened orbital degrees of freedom couple weakly to the impurity spin, driving the system to a FL fixed point. There both spin and orbital degrees of freedom are fully screened, in a manner governed by $SU(6)_1$ fusion rules.

The paper is structured as follows. Section II defines the 3soK model and discusses its weak-coupling renormalization group (RG) flow. Section III presents our NRG results. Section IV gives a synopsis of our CFT results, summarizing all essential insights and arguments, while Sec. V elaborates the corresponding CFT arguments in more detail. Section VI discusses a hybrid Anderson-Kondo model which interpolates between the 3soK model and the 3oAH model. Section VII summarizes our conclusions. The Appendix revisits a two-channel spin-orbital Kondo model studied by Ye in 1997 [48], pointing out the similarities and differences between his work and ours.

II. MODEL, PERTURBATIVE RG FLOW

We study the 3soK model proposed in Ref. [9]. $H_{\text{bath}} = \sum_{p m \sigma} \varepsilon_p \psi_{p m \sigma}^\dagger \psi_{p m \sigma}$ describes a symmetric, flat-band bath, where $\psi_{p m \sigma}^\dagger$ creates an electron with momen-

tum p and spin σ in orbital $m \in \{1, 2, 3\}$. The bath couples to the impurity spin \mathbf{S} and orbital isospin \mathbf{T} via

$$H_{\text{int}} = J_0 \mathbf{S} \cdot \mathbf{J}_{\text{sp}} + K_0 \mathbf{T} \cdot \mathbf{J}_{\text{orb}} + I_0 \mathbf{S} \cdot \mathbf{J}_{\text{sp-orb}} \cdot \mathbf{T}. \quad (1)$$

Here \mathbf{S} are $SU(2)$ generators in the $S = 1$ representation, normalized as $\text{Tr}(S^\alpha S^\beta) = \frac{1}{2} \delta^{\alpha\beta}$, and \mathbf{T} are $SU(3)$ generators in the representation with Young diagram \square , and $\text{Tr}(T^a T^b) = \frac{1}{2} \delta^{ab}$. \mathbf{J}_{sp} , \mathbf{J}_{orb} and $\mathbf{J}_{\text{sp-orb}}$ are the bath spin, orbital and spin-orbital densities at the impurity site, with $J_{\text{sp}}^\alpha = \psi_{m\sigma}^\dagger \frac{1}{2} \sigma_{\sigma\sigma'}^\alpha \psi_{m\sigma'}$, $J_{\text{orb}}^a = \psi_{m\sigma}^\dagger \frac{1}{2} \tau_{mm'}^a \psi_{m'\sigma}$, $J_{\text{sp-orb}}^{\alpha,a} = \psi_{m\sigma}^\dagger \frac{1}{2} \sigma_{\sigma\sigma'}^\alpha \frac{1}{2} \tau_{mm'}^a \psi_{m'\sigma'}$ (summation over repeated indices is implied), where fields are evaluated at the impurity site, $\psi_{m\sigma}^\dagger(r=0)$, and σ^α [τ^a] are Pauli [Gell-Mann] matrices, with normalization $\text{Tr}(\sigma^\alpha \sigma^\beta) = 2\delta^{\alpha\beta}$ [$\text{Tr}(\tau^a \tau^b) = 2\delta^{ab}$]. We use Young diagrams as labels for irreducible representations (irreps) of the $SU(3)$ group. An alternative notation, also frequently used, would be to label $SU(3)$ irreps by their dimension: $\bullet = 1$, $\square = 3$, $\bar{\square} = \bar{3}$, where $\bar{3}$ refers to the conjugate representation of 3 , $\square\square = 6$, $\bar{\square}\bar{\square} = \bar{6}$, $\square\bar{\square} = 8$, etc.

The Hamiltonian has $U(1)_{\text{ch}} \times SU(2)_{\text{sp}} \times SU(3)_{\text{orb}}$ symmetry. We label its symmetry multiplets by $Q = (q, S, \lambda)$, with q the bath particle number relative to half filling (the 3soK impurity has no charge dynamics; hence we may choose $q_{\text{imp}} = 0$), S the total spin, and λ a Young diagram denoting an $SU(3)$ representation. The values of the spin, orbital, and spin-orbital exchange couplings, J_0 , K_0 , I_0 , can be derived from the 3oAH model by a Schrieffer-Wolff transformation [9]. When the 3oAH model is studied in the regime relevant for Hund metals, i.e., with a ferromagnetic on-site Hund coupling J_{H} favoring maximization of the local spin, and with a local filling n_d differing by $\simeq 1$ from half filling, the resulting 3soK exchange couplings J_0 , K_0 , I_0 are typically all positive, i.e., antiferromagnetic. [This can be inferred from Eqs. (4)-(7) of Ref. [9].] Furthermore, when the weak-coupling RG flow of the 3soK model is studied in the presence of finite $K_0 > 0$ and $I_0 > 0$, one finds that J_0 flows toward positive values regardless of whether its initial value is chosen positive or negative [the latter case is illustrated by the purple arrows in Fig. 1(a)]. Hence, we here focus on positive exchange couplings only. However, instead of using values obtained from a Schrieffer-Wolff transformation, here we take the liberty of choosing J_0 , K_0 , I_0 to be independent, tuning them such that $T_{\text{sp}} \ll T_{\text{orb}}$. This is in extension of the 3oAH model, in which T_{sp} is only at most about an order of magnitude smaller than T_{orb} .

Aron and Kotliar [9] have performed a perturbative analysis of the RG flow of the 3soK model. Their Eqs. (8)-(10) describe the flow of the coupling vector, $\mathbf{c}(D) = (J, K, I)$, upon reducing the half-bandwidth D starting from $\mathbf{c}_0 = (J_0, K_0, I_0)$ at D_0 . For the 3soK model, these equations read

$$\begin{aligned} \beta_J &= -(1 - \frac{3}{2}J)(J^2 + \frac{2}{9}I^2) + \dots, \\ \beta_K &= -\frac{3}{2}(1 - K)(K^2 + \frac{1}{2}I^2) + \dots, \\ \beta_I &= -\frac{3}{2}((\frac{4}{3}J + 2K - J^2 - K^2)I - \frac{5}{18}I^2 - \frac{17}{36}I^3) + \dots, \end{aligned} \quad (2)$$

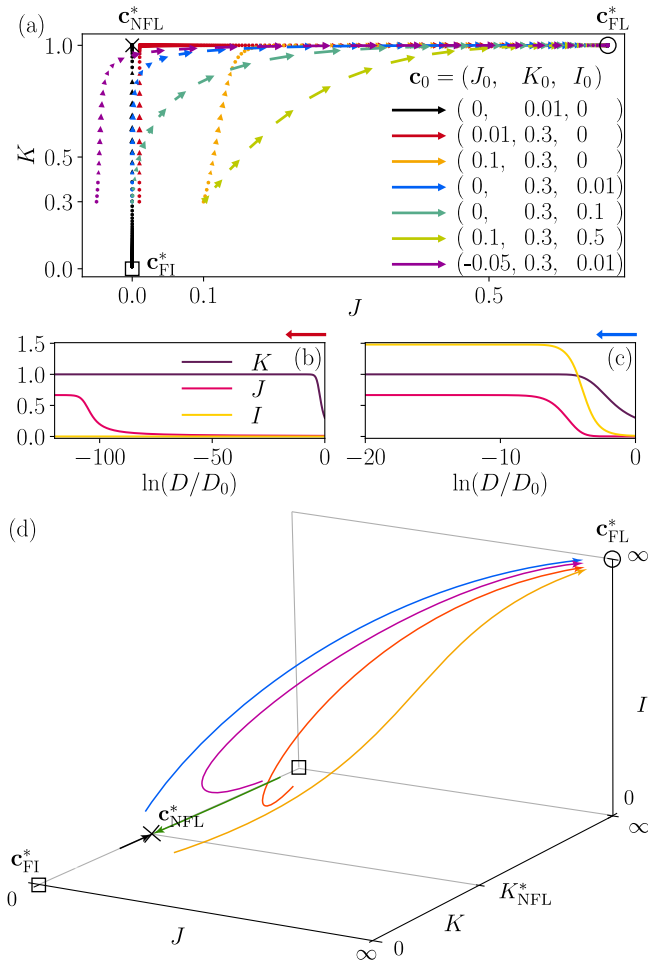


Figure 1. (a) RG flow of the coupling vector $\mathbf{c} = (J, K, I)$ (projected into the J - K plane), obtained by solving the weak-coupling RG equations (2) [Eqs. (8)-(10) of Ref. [9]] for various initial values, $\mathbf{c}_0 = (J_0, K_0, I_0)$. Arrows depict the gradient vector, $-\frac{d}{d \ln D}(J, K)$ at equal steps of $\ln D$. (b),(c) Weak-coupling RG flow of $\mathbf{c}(D)$ for (b) $\mathbf{c}_0 = (0.01, 0.3, 0)$ [red arrows in (a)] and (c) $(0, 0.3, 0.01)$ [blue arrows in (a)]. (d) Qualitative depiction of the conjectured RG flow in the full J - K - I space, for all couplings non-negative. Fat, faint dashed lines show the solutions $\mathbf{c}(D)$ of the weak-coupling equations (2), initialized at $K_0 \ll K_{\text{NFL}}^*$ with $(J_0, I_0) = (0, 0)$ (black), $(> 0, 0)$ (yellow), or $(0, > 0)$ (blue), and plotted only in the weak-coupling regime (beyond the latter, Eqs. (2) lose validity). Solid lines, drawn by hand, qualitatively show the flow expected beyond the weak-coupling regime, including trajectories initialized at $K_0 \gg K_{\text{NFL}}^*$, with $(J_0, I_0) = (0, 0)$ (green), $(> 0, 0)$ (orange), or $(0, > 0)$ (purple). The black squares, cross, and circle depict fixed points.

where $\beta_J = dJ/d \ln D$, etc., with energies in units of D_0 . Figure 1 illustrates the resulting RG flow. There are several fixed points. The free-impurity fixed point, $\mathbf{c}_{\text{FI}}^* = (0, 0, 0)$, is unstable: for any nonzero \mathbf{c}_0 , one or more couplings flow toward strong coupling, and the D values where J or K become of order unity yield estimates of T_{sp} and T_{orb} , respectively. For $\mathbf{c}_0 = (0, K_0 \neq$

$0, 0)$ [black arrows in Fig. 1(a)], the system flows toward a NFL fixed point, $\mathbf{c}_{\text{NFL}}^* = (0, 1, 0)$. This fixed point is unstable against nonzero J_0 or I_0 . For $I_0 = 0$, the flow equations for J and K are decoupled, such that for a small but nonzero $J_0 \ll K_0$ (red arrows) the flow first closely approaches $\mathbf{c}_{\text{NFL}}^*$, until J grows large, driving it toward a FL fixed point \mathbf{c}_{FL}^* . Figure 1(b) shows that the NFL regime ($J \ll K$) governed by $\mathbf{c}_{\text{NFL}}^*$ can be large. For $I_0 \neq 0$, the J and K flows are coupled, hence the growth of K triggers that of J , accelerating the flow toward \mathbf{c}_{FL}^* . In this case, the NFL energy window is rather small [cf. Fig. 1(c)]. For example, for $\mathbf{c}_0 = (0.1, 0.3, 0.5)$ (light green arrows), typical for the values obtained through a Schrieffer-Wolff 3oAH to 3soK mapping, the RG flow does not approach $\mathbf{c}_{\text{NFL}}^*$ very closely; thus fully developed NFL behavior is not observed.

Figure 1(d) offers a qualitative depiction of the conjectured RG flow in the full J - K - I space, for all couplings non-negative. Fat, faint dashed lines show the solutions $\mathbf{c}(D)$ of the weak-coupling Eqs. (2). However, these equations lose validity once the couplings are no longer small (and their above-mentioned predictions that $K_{\text{NFL}}^* = K_{\text{FL}}^* = 1$ should not be trusted). Solid lines, drawn by hand, qualitatively depict the flow expected beyond the weak-coupling regime, based on the following considerations. First, for $K_0 > 0$ and $J_0 = I_0 = 0$, the NRG analysis of Sec. III suggests that the flow proceeds along a trajectory where I and J remain zero, reaching a NFL fixed point, $\mathbf{c}_{\text{NFL}}^* = (0, K_{\text{NFL}}^*, 0)$ at a finite value of K_{NFL}^* . This fixed point is stable, approached by RG flow both from below and above. Correspondingly, the line $J_0 = I_0 = 0$ contains another fixed point at $K_0 = \infty$, which is unstable. To understand the latter point heuristically, consider taking K_0 very large. Then the system will attempt to screen its local orbital degree of freedom, with representation \square , into an orbital singlet. Doing so by binding just a bath single electron, spin up or down, would break spin symmetry. Hence, it must bind two bath electrons, spin up and down, yielding a local orbital degree of freedom yet again, with representation \square . Thus, choosing K_0 very large is equivalent to initializing the model with local orbital representation \square and small initial coupling (presumably $\sim 1/K_0$). This would grow under the RG flow; hence $K_0 = \infty$ is an unstable fixed point, just as $K_0 = 0$. (This argumentation is entirely analogous to that familiar from the two-channel Kondo model [33]; for the present 3soK model, it is further elaborated in Ref. [49].)

For $K_0 > 0$ and J_0, I_0 both non-negative but not both zero, the NRG analysis of Sec. VE suggests that the flow always ends up at a unique FL fixed point \mathbf{c}_{FL}^* . Hence $\mathbf{c}_{\text{NFL}}^*$ is unstable against turning on J_0 or I_0 . The fixed point \mathbf{c}_{FL}^* features a fully screened spin and orbital singlet ground state and an excitation spectrum with $\text{SU}(6)$ symmetry. This implies that as the flow approaches \mathbf{c}_{FL}^* , all three couplings J , K , and I tend to infinity, with relative values such that the fixed-point Hamiltonian has $\text{SU}(6)$ symmetry, i.e., $3J = 2K = I$ [9].

III. NRG RESULTS

To study the RG flow in a quantitatively reliable manner, we solve the 3soK model using NRG [28, 50, 51], exploiting non-Abelian symmetries using QSpace [50]. The bath is discretized logarithmically and mapped to a semi-infinite “Wilson chain” with exponentially decaying hoppings, and the impurity coupled to site 0. The chain is diagonalized iteratively while discarding high-energy states, thereby zooming in on low-energy properties: the (finite-size) level spacing of a chain ending at site k is of order $\omega_k \propto \Lambda^{-k/2}$, where $\Lambda > 1$ is a discretization parameter. The RG flow can be visualized using NRG eigenlevel spectra, showing how the chain’s lowest-lying eigenenergies \mathcal{E} evolve when k is increased by plotting the dimensionless rescaled energies $E = (\mathcal{E} - \mathcal{E}_{\text{ref}})/\omega_k$ versus ω_k for odd k . The E -level flow is stationary (ω_k independent) while ω_k traverses an energy regime governed by one of the system’s fixed points, but changes during crossovers between fixed points.

To analyze the NFL regime in detail, we choose $I_0 = 0$ and $J_0 \ll K_0$, so that the SOS window becomes very large, with $T_{\text{sp}} \ll T_{\text{orb}}$. Figure 2(a) shows the NRG eigenlevel flow diagram for $\mathbf{c}_0 = (10^{-4}, 0.3, 0)$. We discern four distinct regimes, separated by three scales, T_{sp} , T_{ss} , T_{orb} .

- (i) The *free-impurity* (FI) regime, $\omega_k > T_{\text{orb}}$, involves an unscreened impurity, with ground state multiplet $Q = (0, 1, \square)$ (flat brown line).
- (ii) In the NFL regime, $T_{\text{ss}} < \omega_k < T_{\text{orb}}$, two degenerate multiplets, $(1, \frac{1}{2}, \bullet)$ and $(1, \frac{3}{2}, \bullet)$ (dashed green and red lines) become the new ground state multiplets. Below the scale T_{orb} , the impurity orbital isopin is thus screened into an orbital singlet \bullet by binding one bath electron, which couples to the impurity spin 1 to yield a total spin of $\frac{1}{2}$ or $\frac{3}{2}$.
- (iii) In the *spin-splitting* (SS) regime, $T_{\text{sp}} < \omega_k < T_{\text{ss}}$, the effects of nonzero J_0 become noticeable, splitting apart $(1, \frac{1}{2}, \bullet)$ and $(1, \frac{3}{2}, \bullet)$, the latter drifting down.
- (iv) In the FL regime, $\omega_k < T_{\text{sp}}$, $(-2, 0, \bullet)$ becomes the new ground state multiplet. Below the scale T_{sp} , the spin 3/2 is thus screened into a spin singlet by binding three bath holes, yielding a *fully* screened impurity. Note the equidistant level spacing, characteristic of a FL.

To further elucidate the consequences of orbital and spin screening, we computed the impurity’s zero-temperature orbital and spin susceptibilities,

$$\chi_{\text{orb}}^{\text{imp}}(\omega) = -\frac{1}{8\pi} \sum_a \text{Im}\langle T^a \| T^a \rangle_\omega, \quad (3a)$$

$$\chi_{\text{sp}}^{\text{imp}}(\omega) = -\frac{1}{3\pi} \sum_\alpha \text{Im}\langle S^\alpha \| S^\alpha \rangle_\omega, \quad (3b)$$

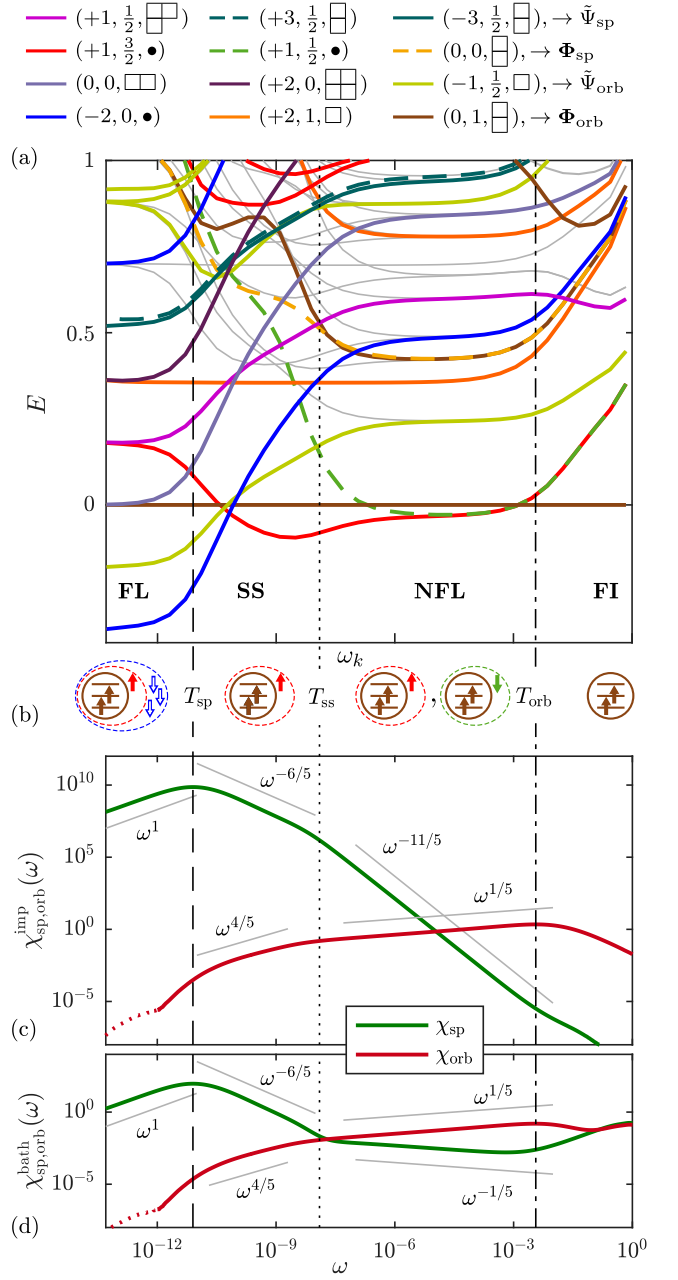


Figure 2. NRG results for $\mathbf{c}_0 = (J_0, K_0, I_0) = (10^{-4}, 0.3, 0)$. (a) Finite-size eigenlevel spectrum computed by NRG, with $\mathcal{E}_{\text{ref}} = \mathcal{E}(0, 1, \square)$ as reference energy. Quantum numbers $Q = (q, S, \lambda)$ are shown at the top, and \rightarrow indicates boundary operators obtained via double fusion. (NRG parameters: $\Lambda = 2.5$; number of kept multiplets, $N_{\text{keep}} = 3000$; half-bandwidth of the bath, $D = 1$.) (b) Illustrations of the ground states encountered during the flow. (c), (d) Imaginary part of the spin and orbital susceptibilities of (c) the impurity and (d) the bath site coupled to it (Wilson chain site $k = 0$). Gray lines show power laws predicted by CFT. Vertical lines show the crossover scales for orbital and spin screening, T_{orb} and T_{sp} , marking the maxima of $\chi_{\text{orb}}^{\text{imp}}$ and $\chi_{\text{sp}}^{\text{imp}}$, and for spin splitting, T_{ss} , marking the kinks in $\chi_{\text{sp,orb}}^{\text{imp,bath}}$.

where $\langle X||X \rangle_\omega$ refers to the Fourier-transformed retarded correlation functions $-i\Theta(t)\langle [X(t), X(0)] \rangle$ with frequency ω , and analogous susceptibilities, $\chi_{\text{orb}}^{\text{bath}}$, $\chi_{\text{sp}}^{\text{bath}}$ (involving \mathbf{J}_{orb} , \mathbf{J}_{sp}) for the bath site coupled to it. To this end we used full-density-matrix (fdm) NRG [52] and adaptive broadening of the discrete NRG data [53].

Figures 2(c) and 2(d) show these susceptibilities on a log-log scale. $\chi_{\text{orb}}^{\text{imp}}$ and $\chi_{\text{sp}}^{\text{imp}}$ each exhibit a maximum, at two widely different scales, T_{orb} and T_{sp} , coinciding with the onset of the stationary NFL or FL regimes in Fig. 2(a), respectively. Moreover, the four susceptibilities $\chi_{\text{orb,sp}}^{\text{imp,bath}}$ all exhibit kinks at a coinciding energy scale, T_{ss} , matching the onset of the SS regime in Fig. 2(a). If ω lies within one of the regimes NFL, SS, or FL, the susceptibilities all show behavior consistent with power laws (gray lines). These power laws can all be explained by CFT, as discussed in Sec. IV. Here we focus on their qualitative features, which by themselves give striking clues about the nature of orbital and spin screening.

In the NFL regime, where $\chi_{\text{orb}}^{\text{imp}}$ decreases with decreasing ω , it exhibits the *same* power law as $\chi_{\text{orb}}^{\text{bath}}$. In this sense, the impurity’s orbital isospin has taken on the same character as that of the bath site it couples to, indicative of orbital screening—in the parlance of AL’s CFT analysis, it has been “absorbed” by the bath. This power law $\omega^{1/5}$ is nontrivial, differing from the ω^1 expected for a fully screened local degree of freedom. This indicates that the local orbital degree of freedom, even while being screened, is still somehow affected by the spin sector. The converse is also true: the onset of orbital screening at T_{orb} is accompanied by a change in behavior for both spin susceptibilities, $\chi_{\text{sp}}^{\text{imp}}$ and $\chi_{\text{sp}}^{\text{bath}}$. Both increase with decreasing ω , with *different* powers, indicative of the absence of spin screening in the NFL regime. The exponent for the impurity spin susceptibility, $\chi_{\text{sp}}^{\text{imp}} \sim \omega^{-11/5}$, is remarkably large in magnitude. (For comparison, for the standard spin-1/2, single-channel Kondo model, $\chi_{\text{sp}}^{\text{imp}} \sim \omega^{-1}$ for $\omega \gtrsim T_{\text{sp}}$.) The highly singular $\omega^{-11/5}$ behavior—our perhaps most unexpected result—indicates that the strength of spin fluctuations is strongly amplified by the onset of orbital screening. Our CFT analysis below will reveal the reason for this: orbital screening is accompanied by a renormalization of the local bath spin density at the impurity site.

Upon entering the SS regime, all susceptibility lines show a kink, i.e., change in power law, such that the impurity and bath exponents match not only in the orbital sector, $\chi_{\text{orb}}^{\text{imp}} \sim \chi_{\text{orb}}^{\text{bath}}$, but now also in the spin sector, $\chi_{\text{sp}}^{\text{imp}} \sim \chi_{\text{sp}}^{\text{bath}}$. The latter fact indicates clearly that bath and impurity spin degrees of freedom have begun to interact with each other. However, this is only a precursor to spin screening, since the spin susceptibilities still increase with decreasing ω , albeit with a smaller exponent, $\chi_{\text{sp}}^{\text{imp,bath}} \sim \omega^{-6/5}$, than in the NFL regime. However, since the exponent $\gamma = 6/5$ is larger than 1, spin fluctuations are anomalously large also in this regime. Importantly, this regime persists also for parameters corresponding to the more realistic 3oAH model. Indeed,

previous DMFT studies for a self-consistent 3oAH model have yielded behavior for $\chi_{\text{sp}}^{\text{imp}}$ which in the SOS regime is consistent with an exponent of $\gamma = 6/5$, as further discussed in Secs. IV and VI. Moreover, as mentioned in the Introduction, anomalously large spin fluctuations are of direct relevance for the superconducting state of the iron pnictide Hund metals: in Ref. [14], strong spin fluctuations with $\gamma > 1$ were a key ingredient for a proposed explanation for the anomalously large ratio of $2\Delta_{\text{max}}/T_c$ observed experimentally.

Full spin screening eventually sets in in the FL regime, where the spin susceptibilities $\chi_{\text{sp}}^{\text{imp,bath}}$ show the ω^1 behavior characteristic of a FL. We expect this behavior also for the orbital susceptibilities, but have not been able to observe it directly, since our results for $\chi_{\text{orb}}^{\text{imp,bath}}$ become numerically unstable when dropping below $\simeq 10^{-5}$ [as indicated by dotted lines in Figs. 2(c) and (d)].

In the following two sections we explain how the above NRG results can be understood using CFT arguments.

IV. CFT ANALYSIS: SYNOPSIS

This section presents a synopsis of our CFT analysis. It aims to be accessible also to readers without in-depth knowledge of AL’s CFT work on Kondo models. We begin by summarizing AL’s strategy for analyzing strong-coupling fixed points of quantum impurity models (Sec. IV A). We then apply it to the NFL fixed point (Sec. IV B) and the FL fixed point (Sec. IV C). A more elaborate discussion of CFT details follows in Sec. V.

A. General strategy

AL’s strategy for determining spectra and correlation functions from CFT involves three key concepts:

- (C1) *Independent excitations.*—The starting assumption is that the low-energy spectrum of a multiorbital Kondo Hamiltonian at a conformally invariant fixed point can be constructed from combinations of *independent* charge, spin, and orbital excitations. The excitation energies in each sector follow from the commutation relations of certain charge, spin, and orbital operators (these form a so-called Kac-Moody algebra); this is expressed in Eqs. (4) and (12).
- (C2) *Gluing conditions and fusion rules.*—The spectrum of excitations in each sector (charge, spin, orbital) is the same at the free and strong-coupling fixed points. However, the way in which these three types of excitations should be combined to obtain valid many-body excitations, specified by so-called *gluing conditions*, differs for the free and strong-coupling fixed points. At the former, excitations are glued together in such a manner that a free-fermion spectrum is recovered. At the latter, the

Table I. Left: Five low-lying free-fermion multiplets (|FS) denotes the Fermi sea), with quantum numbers (q, S, λ) , multiplet dimensions d , and energies $E(q, S, \lambda)$. Center: “Single fusion” with an impurity $Q_{\text{imp}} = (0, 1, \square)$ leads to multiplets with quantum numbers (q, S', λ') , dimensions d' , eigenenergies $E' = E(q, S, \lambda')$, and excitation energies $\delta E' = E' - E'_{\text{min}}$. Right: “Double fusion,” which fuses multiplets from the middle column with an impurity in the conjugate representation $\bar{Q}_{\text{imp}} = (0, 1, \square)$ [cf. Sec. VB, details on (C3)], yields the multiplets (q, S'', λ'') . These characterize the CFT boundary operators \hat{O} , with scaling dimensions $\Delta = E(q, S, \lambda'')$. Φ_{orb} and Φ_{sp} are the leading boundary operators in the orbital and spin sectors, respectively. In the spin-splitting regime, their roles are taken by $\tilde{\Psi}_{\text{orb}}$ and $\tilde{\Psi}_{\text{sp}}$, respectively. “Bare” free-fermion versions of these boundary operators, having the same quantum numbers, are listed on the very right. For clarity, not all possible multiplets arising from single and double fusion are shown. A more comprehensive list is given in Table II.

Free fermions					Single fusion					Double fusion						
State	q	S	λ	d	E	q	S'	λ'	d'	$\delta E'$	q	S''	λ''	Δ	\hat{O}	\hat{O}_{bare}
FS)	0	0	•	1	0	0	1	\square	9	$\frac{1}{30}$	0	0	\square	$\frac{3}{5}$	Φ_{orb}	$\mathbf{T}, \mathbf{J}_{\text{orb}}$
$\psi_{m\sigma}^\dagger$ FS)	1	$\frac{1}{2}$	\square	6	$\frac{1}{2}$	1	$\{\frac{1}{2}, \frac{3}{2}\}$	•	6	0
$\psi_{m\sigma}$ FS)	-1	$\frac{1}{2}$	\square	6	$\frac{1}{2}$	-1	$\frac{1}{2}$	\square	6	$\frac{4}{15}$	-1	$\frac{1}{2}$	\square	$\frac{9}{10}$	$\tilde{\Psi}_{\text{orb}}$	$(\psi_{l\sigma}^\dagger \psi_{l\sigma} - \psi_{m\sigma}^\dagger \psi_{m\sigma}) \psi_{n\sigma},$ $\psi_{l\sigma}^\dagger \psi_{m\sigma} \psi_{n\sigma}, l \neq m \neq n$
$\mathbf{J}_{\text{sp-orb}}$ FS)	0	1	\square	24	1	0	0	\square	3	$\frac{13}{30}$	0	1	•	$\frac{2}{5}$	Φ_{sp}	\mathbf{J}_{sp}
...	-3	$\frac{1}{2}$	\square	16	$\frac{3}{2}$	-3	$\frac{1}{2}$	\square	6	$\frac{14}{15}$	-3	$\frac{1}{2}$	•	$\frac{9}{10}$	$\tilde{\Psi}_{\text{sp}}$	$\psi_{1\sigma} \psi_{2\sigma} \psi_{3\bar{\sigma}}$

impurity has been absorbed by the bath, implying changes in the gluing conditions relative to those of the free fixed point. These changes are governed by so-called *fusion rules*, which specify how the impurity degrees of freedom should be “added” to those of the bath. This is conceptually similar to angular momentum addition, but with additional constraints to respect the Pauli principle.

(C3) *Scaling dimensions*.—Once the fusion rules and thus the spectrum of valid many-body excitations is known, the conformal scaling dimensions of operators living at the impurity site can be determined by using the same fusion rules once more (“double fusion”). Because of conformal invariance, the functional form of correlation functions is fully determined by the scaling dimensions of their operators.

In practice, analyzing a conformally invariant strong-coupling fixed point thus consists of three steps: (C1) determine the independent excitations, (C2) use “single fusion” to obtain the strong-coupling gluing conditions, and (C3) use “double fusion” to obtain the scaling dimensions of operators living at the impurity site. Even though AL’s justification of this strategy involved sophisticated CFT arguments, its application to an actual model is rather straightforward, once one has determined the appropriate fusion rules. For the 3soK model, we present tables with the explicit fusion rules in the Supplemental Material (SM) [54], and Table II shows details on the fusion procedure. These tables are also meant to serve as a guide for future applications of AL’s methodology.

B. NFL regime

In the following, we follow this strategy for the NFL fixed point of the 3soK model.

(C1) The 3soK model, being spherically symmetric around the origin, describes an effectively one-dimensional system. In the imaginary-time formalism, the field describing the conduction band, $\psi(\tau + ir)$, lives on the upper half of the complex plane, with time, τ , on the real and the distance, r , from the impurity on the imaginary axis. The impurity at $r = 0$ constitutes a “boundary” at the real axis. The fixed points of the model, assumed to be scale invariant, can thus be described using (1+1)-dimensional boundary CFT.

The bath of the 3soK model trivially has $U(1) \times SU(2) \times SU(3)$ symmetry. Moreover, since we assumed a flat band, i.e., a linear dispersion, it also has conformal symmetry. The combination of both leads to the symmetry $U(1) \times SU(2)_3 \times SU(3)_2$, where $SU(2)_3$ and $SU(3)_2$ refer to generalizations of the familiar $SU(2)$ and $SU(3)$ algebras, known as Kac-Moody algebras [44, 57, 58]. The subscript on $SU(2)_3$ states that only those spin representations are allowed which can be constructed from electrons living on 3 orbitals. In particular, spins larger than $3/2$ do not occur in this algebra. The subscript on $SU(3)_2$ indicates analogous restrictions for the allowed $SU(3)$ representations. (The consequences of these restrictions are made explicit in Tables S3 and S2 of the Supplemental Material [54].)

According to AL [42–46], the fixed points can be analyzed as follows. First, standard $U(1) \times SU(2)_3 \times SU(3)_2$ non-Abelian bosonization is used to decompose the bath Hamiltonian into charge, spin, and orbital contributions,

$$H_{\text{bath}} \sim \int dr \left(\frac{1}{12} J_{\text{ch}}^2(r) + \frac{1}{5} \mathbf{J}_{\text{sp}}^2(r) + \frac{1}{5} \mathbf{J}_{\text{orb}}^2(r) \right), \quad (4)$$

with $J_{\text{ch}}(r) = \psi_{m\sigma}^\dagger(r) \psi_{m\sigma}(r)$, etc. (We omitted overall

prefactors; for a detailed discussion, see Refs. [44, 57].) Since J_{ch} , \mathbf{J}_{sp} , \mathbf{J}_{orb} are generators of the $U(1)$, $SU(2)_3$, $SU(3)_2$ Kac-Moody algebras, respectively, the eigenstates of H_{bath} can be organized into multiplets forming irreps of the corresponding symmetry groups, labeled by quantum numbers $Q_{\text{bath}} = (q, S, \lambda)$. If the bath is put in a box of finite size, the corresponding free-fermion excitation eigenenergies $E(q, S, \lambda)$ are discrete and simple functions of the quantum numbers [see Eq. (12)].

(C2) Next, we include the interaction with the impurity in the orbital sector ($K_0 > 0$, $J_0 = I_0 = 0$) to describe the properties of the NFL fixed point $\mathbf{c}_{\text{NFL}}^*$. The bosonized H_{bath} is quadratic in \mathbf{J}_{orb} , whereas the coupling term $H_{\text{int}} = K_0 \mathbf{T} \cdot \mathbf{J}_{\text{orb}}(r=0)$ is linear. The latter can thus be absorbed into the former, in the spirit of “completing the square.” AL conjectured that at the strong-coupling fixed point, this replacement takes the form

$$\mathbf{J}_{\text{orb}}(r) \mapsto \mathcal{J}_{\text{orb}}(r) = \mathbf{J}_{\text{orb}}(r) + \delta(r) \mathbf{T}, \quad (5)$$

with \mathcal{J}_{orb} satisfying the same Kac-Moody algebra as \mathbf{J}_{orb} . At the strong-coupling fixed point, the Hamiltonian can thus be expressed as $H = H_{\text{bath}}[\mathbf{J}_{\text{orb}}] + H_{\text{int}} = H_{\text{bath}}[\mathcal{J}_{\text{orb}}]$ (more details can be found in Sec. VB and Ref. [43]).

It follows immediately that at the fixed point, the spectrum of irreps of the full Hamiltonian can be obtained by combining the irreps of bath and impurity degrees of freedom, $Q_{\text{bath}} \otimes Q_{\text{imp}} = \sum_{\oplus} Q'$, and using “fusion rules” to deduce the resulting irreps Q' . This is conceptually similar to coupling two $SU(2)$ spins, $\mathbf{S}'' = \mathbf{S} + \mathbf{S}'$, decomposing the direct product of their irreps as $S \otimes S' = \sum_{\oplus} S''$, and deducing that S'' ranges from $|S - S'|$ to $S + S'$. However, in the present context, specific assumptions must be made about which degrees of freedom are involved in the screening processes and which are not, and for those which are, Kac-Moody fusion rules have to be used when combining irreps. For the present situation, we have $Q_{\text{bath}} = (q, S, \lambda)$ and $Q_{\text{imp}} = (0, 1, \square)$, and place ourselves *at* the NFL fixed point, where bath and impurity couple only in the orbital sector.

To find the allowed irreps $Q' = (q', S', \lambda')$, we therefore posit the following fusion strategy (inspired by and generalizing that of AL [42–46]). In the charge sector, $q_{\text{imp}} = 0$ trivially implies that $q' = q$. In the orbital sector, the impurity’s orbital isospin is coupled to that of the bath [Eq. (1)] and absorbed by it according to Eq. (5); hence, $\lambda \otimes \lambda_{\text{imp}} = \sum_{\oplus} \lambda'$ is governed by the fusion rules of the $SU(3)_2$ Kac-Moody algebra. By contrast, in the spin sector the impurity spin is a spectator, decoupled from the bath (we are *at* $\mathbf{c}_{\text{NFL}}^*$, where $J_0 = I_0 = 0$); hence, $S \otimes S_{\text{imp}} = \sum_{\oplus} S'$ is governed by the fusion rules of the $SU(2)$ Lie algebra [not the $SU(2)_3$ Kac-Moody algebra]. The set of excitations (q, S', λ') so obtained have energies given by $E(q, S, \lambda')$, not $E(q, S', \lambda')$, since H_{int} only acts in the orbital sector. A more complete discussion of our “fusion hypothesis” is given in Sec. VB. The resulting spectrum reproduces the NRG spectrum in the

NFL fixed point regime (see Table II).

Table I exemplifies a few many-body states obtained via this fusion scheme (AL called it single fusion, in distinction from a second fusion step, discussed below). In particular, the degenerate ground state multiplets of $\mathbf{c}_{\text{NFL}}^*$, $(1, \frac{1}{2}, \bullet)$ and $(1, \frac{3}{2}, \bullet)$ [cf. Fig. 2(a)], arise via fusion of a one-particle bath excitation, $(+1, \frac{1}{2}, \square)$, with the impurity, $(0, 1, \square)$, schematically depicted in Fig. 2(b).

(C3) Next, we want to compute the leading scaling behavior of spin and orbital correlation functions at the impurity site, i.e., on the boundary of the CFT. The absorption of the impurity into the bath (bulk) Hamiltonian translates, in CFT language, to a change in the boundary condition imposed on the theory at $r=0$. As a result, a new set of “boundary operators,” i.e., local operators living at the impurity site, appear in the theory. These fully characterize the strong-coupling fixed point. Each boundary operator can be viewed as the renormalized version, resulting from the screening process, of some bare local operator having the same quantum numbers.

According to AL, the boundary operators can be obtained via a second fusion step (double fusion) (cf. Refs. [44–46] and Appendix C of Ref. [57]). Each multiplet (q, S'', λ'') resulting from double fusion is associated with a boundary operator \hat{O} with the same quantum numbers, and a scaling dimension given by $\Delta = E(q, S, \lambda'')$ (cf. Table I). The realization that the scaling dimensions of boundary operators are related to finite-size excitation energies is due to Cardy [59]. Using a conformal mapping, he mapped the complex upper half-plane to a strip of infinite length and finite width, in such a way that the nontrivial boundary condition of the half-plane is mapped to both boundaries of the strip. He then showed that the boundary operators of the half-plane and their scaling dimensions can be associated with the finite-size spectrum of a Hamiltonian defined along the width of this strip. Since the strip has two nontrivial boundaries, one on each side, the finite-size spectrum can be found using a double-fusion procedure. The scaling dimensions of the boundary operators fully determine their time- or frequency-dependent correlators, $\langle \hat{O}(t) \hat{O}(0) \rangle \sim t^{-2\Delta}$ and $\langle \hat{O} || \hat{O} \rangle_{\omega} \simeq \omega^{2\Delta-1}$.

To explain the power laws found in the NFL regime of Figs. 2(c) and 2(d), and particularly the fact that there $\chi_{\text{orb}}^{\text{imp}}$ and $\chi_{\text{orb}}^{\text{bath}}$ exhibit the *same* power law, while $\chi_{\text{sp}}^{\text{imp}}$ and $\chi_{\text{sp}}^{\text{bath}}$ do not, we posit that the local operators in the orbital and spin exchange terms of Eq. (1) are renormalized to

$$\mathbf{J}_{\text{orb}} \mapsto \Phi_{\text{orb}}, \quad \mathbf{T} \mapsto \Phi_{\text{orb}}, \quad \mathbf{J}_{\text{sp}} \mapsto \Phi_{\text{sp}}, \quad \mathbf{S} \mapsto \mathbf{S}. \quad (6)$$

Here Φ_{orb} has quantum numbers $(0, 0, \square)$ (same as \mathbf{T} , \mathbf{J}_{orb}) and dimension $\Delta_{\text{orb}} = \frac{3}{5}$, while Φ_{sp} has quantum numbers $(0, 1, \bullet)$ (same as \mathbf{S} , \mathbf{J}_{sp}) and $\Delta_{\text{sp}} = \frac{2}{5}$, (cf. Table I). The local impurity and bath orbital susceptibilities thus both scale as

$$\chi_{\text{orb}}^{\text{imp, bath}} \sim \langle \Phi_{\text{orb}} || \Phi_{\text{orb}} \rangle_{\omega} \sim \omega^{2\Delta_{\text{orb}}-1} = \omega^{1/5}, \quad (7)$$

and the bath spin susceptibility as

$$\chi_{\text{sp}}^{\text{bath}} \sim \langle \Phi_{\text{sp}} | \Phi_{\text{sp}} \rangle_{\omega} \sim \omega^{2\Delta_{\text{sp}}-1} = \omega^{-1/5}. \quad (8)$$

By contrast, the impurity spin \mathbf{S} is not renormalized, because *at* the fixed point $\mathbf{c}_{\text{NFL}}^*$, where $J_0 = 0$, it is decoupled from the bath. Thus its scaling dimension is zero. The leading behavior of $\chi_{\text{sp}}^{\text{imp}}$ is obtained by now taking $J_0 \neq 0$ but very small ($\ll K_0$), and doing second-order perturbation theory in the renormalized spin exchange interaction. Thus, $\chi_{\text{sp}}^{\text{imp}}$ is proportional to the Fourier transform of $\langle \mathbf{S}(t)\mathbf{S}(0) \rangle$ ($\int dt' J_0 \mathbf{S} \cdot \Phi_{\text{sp}}^2$), and power counting yields

$$\chi_{\text{sp}}^{\text{imp}} \sim \omega^{2\Delta_{\text{sp}}-3} = \omega^{-11/5}. \quad (9)$$

The above predictions are all borne out in Figs. 2(c) and 2(d).

The remarkably large negative exponent, $-\frac{11}{5}$, for $\chi_{\text{sp}}^{\text{imp}}$ reflects the fact that the renormalized spin exchange interaction $J_0 \mathbf{S} \cdot \Phi_{\text{sp}}$, with scaling dimension $\frac{2}{5} < 1$, is a relevant perturbation. Its strength, though initially miniscule if $J_0 \ll 1$, grows under the RG flow, causing a crossover away from $\mathbf{c}_{\text{NFL}}^*$ for $\omega \lesssim T_{\text{ss}}$. This is reflected in the level crossings around T_{ss} in the NRG eigenlevel flow of Fig. 2. In particular, the double-fusion parent multiplets for Φ_{orb} and Φ_{sp} , namely $(0, 1, \square)$ and $(0, 0, \square)$, undergo level crossings with the downward-moving multiplets $(-1, \frac{1}{2}, \square)$ and $(-3, \frac{1}{2}, \square)$, respectively. These in turn are double-fusion parent multiplets for the boundary operators $\tilde{\Psi}_{\text{orb}}$ and $\tilde{\Psi}_{\text{sp}}$, with scaling dimensions $\tilde{\Delta}_{\text{orb}} = \tilde{\Delta}_{\text{sp}} = \frac{9}{10}$ (Table I). To explain the SS regime of Figs. 2(c) and 2(d), and particularly that there the power laws for χ^{imp} and χ^{bath} match in both the orbital *and* spin sectors, we posit the RG replacements

$$\mathbf{J}_{\text{orb}} \mapsto \tilde{\Psi}_{\text{orb}}, \quad \mathbf{T} \mapsto \tilde{\Psi}_{\text{orb}}, \quad \mathbf{J}_{\text{sp}} \mapsto \mathbf{S} + \tilde{\Psi}_{\text{sp}}, \quad \mathbf{S} \mapsto \mathbf{S} + \tilde{\Psi}_{\text{sp}}.$$

Here $\mathbf{S} + \tilde{\Psi}_{\text{sp}}$ is symbolic notation for some linear admixture of both operators, induced by the action of the renormalized spin exchange interaction. We thus obtain

$$\chi_{\text{orb}}^{\text{imp,bath}} \sim \langle \tilde{\Psi}_{\text{orb}} | \tilde{\Psi}_{\text{orb}} \rangle_{\omega} \sim \omega^{2\tilde{\Delta}_{\text{orb}}-1} = \omega^{4/5}, \quad (10)$$

and the leading contribution to $\chi_{\text{sp}}^{\text{imp}}$ and $\chi_{\text{sp}}^{\text{bath}}$, obtained by perturbing $\langle \mathbf{S}(t)\mathbf{S}(0) \rangle$ to second order in $\mathbf{S}\tilde{\Psi}_{\text{sp}}$ [60], is

$$\chi_{\text{sp}}^{\text{imp,bath}} \sim \omega^{2\tilde{\Delta}_{\text{sp}}-3} = \omega^{-6/5}. \quad (11)$$

This reproduces the power laws found in Figs. 2(c) and 2(d).

Remarkably, $\chi_{\text{sp}}^{\text{imp}} \sim \omega^{-6/5}$ behavior has also been found in studies of the self-consistent 3oAH model arising in our DMFT investigations of the three-orbital Hubbard-Hund model for Hund metals. For the 3oAH model the spin-orbital coupling I_0 in Eq. (1) is always nonzero, so that a fully fledged NFL does not emerge—instead, T_{orb} and T_{ss} effectively coincide (as further discussed in Sec. VI). However, the SS regime between T_{sp}

and $T_{\text{ss}} \simeq T_{\text{orb}}$ can be quite wide, typically at least an order of magnitude. In Fig. 3(c) of Ref. [22], the behavior of $\chi_{\text{sp}}^{\text{imp}}$ in this regime (between the vertical solid and black lines there) is consistent with $\omega^{-6/5}$ behavior. Though this fact was not noted in Ref. [22], it was subsequently pointed out in Ref. [14] (see Fig. S1 of their Supplemental Material). Behavior consistent with $\chi_{\text{sp}}^{\text{imp}} \sim \omega^{-6/5}$ can also be seen in Figs. 5.1(c) and 5.1(d) of Ref. [47], as discussed on p. 152 therein. The explanation for this behavior presented here, via a CFT analysis of the NFL and SS regimes, is one of the main results of this work, and the justification for the first part of the title of this paper.

C. Fermi-liquid regime

As mentioned above, the low-energy regime below T_{sp} is a FL. The fixed-point spectrum at \mathbf{c}_{FL}^* can be obtained by fusing a free-fermion spectrum with an impurity with $Q_{\text{imp}} = (1, \frac{3}{2}, \bullet)$, representing the effective local degree of freedom obtained after completion of orbital screening (see Table III). Since the ground state describes a fully screened orbital and spin singlet, it actually is the singlet of a larger symmetry group, $U(1) \times SU(6)$. Indeed, the fixed-point spectrum at \mathbf{c}_{FL}^* matches that of the $U(1) \times SU(6)$ symmetric Kondo model. We demonstrate this, using both NRG and CFT with $SU(6)_1$ fusion rules, in Sec. VE (see Table IV). The FL nature of the ground state is also borne out by the ω^1 scaling of $\chi_{\text{sp}}^{\text{imp,bath}}$ in the FL regime of Figs. 2(c) 2(d).

V. CFT ANALYSIS: DETAILS

We now provide technical details for our CFT analysis of the NFL and FL fixed points of the three-orbital Kondo (3soK) model discussed in Secs. III and IV. We closely follow the strategy devised by Affleck and Ludwig for their pioneering treatment of the strong-coupling fixed points of Kondo models [42–46] (for pedagogical reviews, see Refs. [58, 61] and Appendixes A–D of Ref. [57]). In a series of works, they considered a variety of Kondo models of increasing complexity. These include the standard one-channel, $SU(2)$ spin Kondo model with a spin exchange interaction between bath and impurity with $U(1) \times SU(2)_1$ symmetry; a spinful k -channel bath coupled to an $SU(2)$ impurity [$U(1) \times SU(2)_k \times SU(k)_2$ symmetry], and an $SU(N)$ k -channel bath coupled to an $SU(N)$ impurity [$U(1) \times SU(N)_k \times SU(k)_N$ symmetry].

Our 3soK model features a spinful three-channel bath and an $SU(2)_{\text{sp}} \times SU(3)_{\text{orb}}$ impurity [$U(1) \times SU(2)_3 \times SU(3)_2$ symmetry]. The impurity multiplet is a direct product of a spin triplet ($S = 1$) and an orbital triplet ($\lambda = \square$). Its direct-product structure is more general than any of the cases considered by AL. (A two-channel version of our model, with $U(1) \times SU(2)_2 \times SU(2)_2$ symmetry, has been studied by Ye [48], which we discuss in

the Appendix.) However, at the NFL fixed point $\mathbf{c}_{\text{NFL}}^*$ of our model, where $J_0 = I_0 = 0$, the impurity's $\text{SU}(2)$ spin is a decoupled, threefold degenerate spectator degree of freedom. Hence AL's analysis [46] can be employed, with $N = 3$ and $k = 2$ channels, modulo some minor changes to account for the impurity spin.

By contrast, in the spin-splitting crossover regime the spin exchange interaction comes to life, so that the impurity's $\text{SU}(2)$ spin degrees of freedom cease to be mere spectators. This regime thus lies outside the realm of cases studied by AL; in particular, it is not manifestly governed by the NFL fixed point $\mathbf{c}_{\text{NFL}}^*$, or any other well-defined fixed point. Correspondingly, our discussion of this crossover regime in Sec. VC2 is more speculative than that of the NFL regime, though our heuristic arguments are guided by and consistent with our NRG results.

Finally, for our model's FL fixed point \mathbf{c}_{FL}^* , we are again in well-chartered territory: it can be understood by applying AL's strategy to an $\text{SU}(6)$ one-channel bath coupled to an $\text{SU}(6)$ impurity [$\text{U}(1) \times \text{SU}(6)_1$ symmetry].

Below we assume the reader to be familiar with AL's work and just focus on documenting the details of our analysis. Section VA describes how the free-fermion bath spectrum is decomposed into charge, spin, and orbital excitations using $\text{U}(1) \times \text{SU}(2)_3 \times \text{SU}(3)_2$ non-Abelian bosonization. Section VB derives the finite-size spectrum and boundary operators of the NFL fixed point via single and double fusion, using the fusion rules of the $\text{SU}(3)_2$ Kac-Moody algebra in the orbital sector and the $\text{SU}(2)$ Lie algebra in the spin sector. Section VC describes the computation of the spin and orbital susceptibilities in the NFL and SS regimes, linking AL's strategy for computing such quantities to the compact scaling arguments used in Sec. IV. Section VD presents our results for the impurity spectral function in the NFL regime. Finally, Sec. VE, devoted to the FL regime, shows how its spectrum can be derived using either $\text{SU}(2)_3$ fusion rules in the spin sector or $\text{SU}(6)_1$ fusion rules in the flavor (combined spin+orbital) sector.

A. Non-Abelian $\text{U}(1) \times \text{SU}(2)_3 \times \text{SU}(3)_2$ bosonization

(C1) The first step of AL's CFT approach for multi-channel Kondo models is to use non-Abelian bosonization to decompose the bath degrees of freedom into charge, spin, and orbital excitations in a manner respecting the symmetry of the impurity-bath exchange interactions. Our 3soK model features a spinful three-channel bath, with $H_{\text{bath}} = \sum_{p m \sigma} \varepsilon_p \psi_{p m \sigma}^\dagger \psi_{p m \sigma}$. We assume a linear dispersion, $\varepsilon_p = \hbar v_{\text{F}} p$, with $\hbar v_{\text{F}} = 1$. Using non-Abelian bosonization with the $\text{U}(1) \times \text{SU}(2)_3 \times \text{SU}(3)_2$ Kac-Moody (KM) current algebra, the spectrum of bath excitations can be expressed as (see Refs. [42, 44], or Appendix A of

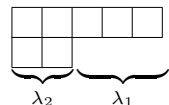
Ref. [57])

$$E(q, S, \lambda) = \frac{1}{12} q^2 + \frac{1}{5} \kappa_2(S) + \frac{1}{5} \kappa_3(\lambda) + \ell, \quad (12a)$$

$$\kappa_2(S) = S(S+1), \quad (12b)$$

$$\kappa_3(\lambda) = \frac{1}{3} (\lambda_1^2 + \lambda_2^2 + \lambda_1 \lambda_2 + 3\lambda_1 + 3\lambda_2). \quad (12c)$$

Here $\kappa_2(S)$ and $\kappa_3(\lambda)$ are the eigenvalues of the quadratic Casimir operators of the $\text{SU}(2)$ and $\text{SU}(3)$ Lie algebras, respectively [62]. $q \in \mathbb{Z}$ is the $\text{U}(1)$ charge quantum number, $S \in \frac{1}{2}\mathbb{Z}$ the $\text{SU}(2)$ spin quantum number, and $\lambda = (\lambda_1, \lambda_2)$ the $\text{SU}(3)$ orbital quantum number, denoting a Young diagram with λ_j j -row columns:



$$\begin{array}{l} \lambda_1 = \text{number of one-row columns} \\ \lambda_2 = \text{number of two-row columns} \end{array}$$

Finally, $\ell \in \mathbb{Z}$ counts higher-lying ‘‘descendent’’ excitations; for present purposes it suffices to set $\ell = 0$.

The free-fermion spectrum of H_{bath} is recovered from Eq. (12a) by imposing free-fermion ‘‘gluing conditions,’’ allowing only those combinations of quantum numbers (q, S, λ) for which $E(q, S, \lambda)$ is an integer multiple of $1/2$. The resulting multiplets are listed in the left-hand column (‘‘Free fermions’’) of Table II.

B. Non-Fermi-liquid fixed point

(C2) We now focus on the NFL fixed point of the 3soK model, at $\mathbf{c}_{\text{NFL}}^*$, where $(J_0, K_0, I_0) = (0, 1, 0)$. According to AL's general strategy, the orbital isospin T can be then ‘‘absorbed’’ by the bath through the substitution

$$\mathbf{J}_{\text{orb}, n} \mapsto \mathcal{J}_{\text{orb}, n} = \mathbf{J}_{\text{orb}, n} + \mathbf{T}. \quad (13)$$

Here $\mathbf{J}_{\text{orb}, n}$ and $\mathcal{J}_{\text{orb}, n}$ are Fourier components (n being a Fourier index) of the bare and bulk orbital isospin currents, respectively, defined for a bath in a finite-sized box. (The local bath operator \mathbf{J}_{orb} is proportional to $\sum_{n \in \mathbb{Z}} \mathbf{J}_{\text{orb}, n}$.) The right-hand side of Eq. (13) is reminiscent of the addition of Lie algebra generators, $\mathbf{S}' = \mathbf{S} + \tilde{\mathbf{S}}$, when performing a direct product decomposition, $\mathbf{S} \otimes \tilde{\mathbf{S}} = \sum_{\oplus} \mathbf{S}'$, of $\text{SU}(2)$ multiplets. The terms added in Eq. (13), however, generate two *different* algebras: $\mathbf{J}_{\text{orb}, n}$ are generators of the $\text{SU}(3)_2$ KM algebra, \mathbf{T} of the $\text{SU}(3)$ Lie algebra. AL proposed a remarkable fusion hypothesis for dealing with such situations (and confirmed its veracity by detailed comparisons to Bethe ansatz and NRG computations). For the present context their fusion hypothesis states: the eigenstates of the combined bath+impurity system can be obtained by combining (or ‘‘fusing’’) their orbital degrees of freedom, $\lambda \otimes \lambda_{\text{imp}} = \sum_{\oplus} \lambda'$, using the fusion rules of the $\text{SU}(3)_2$ KM algebra, as though the impurity's orbital multiplet were an $\text{SU}(3)_2$, not $\text{SU}(3)$, multiplet. The $\text{SU}(3)_2$ fusion rules are depicted in Table S2 of the Supplemental Material [54].

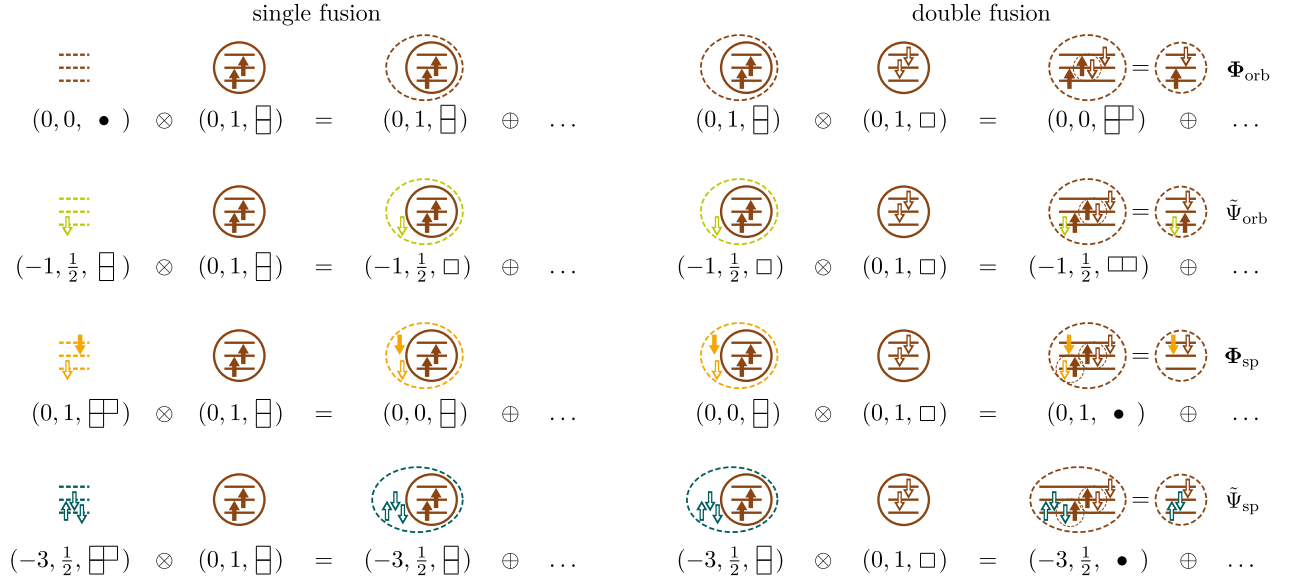


Figure 3. Schematic depiction of single fusion (left) and double fusion (right), for the four multiplets giving rise to the boundary operators Φ_{orb} , Φ_{sp} , $\tilde{\Psi}_{\text{orb}}$, $\tilde{\Psi}_{\text{sp}}$ discussed in Sec. IV (corresponding to rows 1,3,4,5 in Table I). Filled arrows represent electrons, empty arrows represent holes. An electron with spin \uparrow and a hole with spin \downarrow (missing electron with spin \uparrow) can be combined to annihilate each other, as indicated by small dashed circles in the last column. Our illustrations depict the impurity using a fermionic representation, as would be appropriate for the 3oAH model, even though the 3soK impurity has no charge dynamics. In the “single fusion” column, excitations of the free bath are fused with the impurity, $Q_{\text{imp}} = (0, 1, \square)$, to obtain the eigenmultiplets of the full system at the NFL fixed point. In the “double fusion” column (right), the single-fusion results are fused with the conjugate impurity representation, $\bar{Q}_{\text{imp}} = (0, 1, \square)$. Each of the resulting multiplets is associated with a boundary operator having the same quantum numbers. Colors relate the multiplets obtained after single fusion to the corresponding lines in Fig. 2.

Table II. Fusion table for orbital screening at the NFL fixed point $\mathbf{c}_{\text{NFL}}^*$ of the 3soK model. Left: The 14 lowest low-lying free-fermion multiplets (q, S, λ) , with multiplet dimensions d and energies $E(q, S, \lambda)$, computed using Eqs. (12) and Table S1 of the SM [54]. Center: Single fusion with a $Q_{\text{imp}} = (0, 1, \square)$ impurity, using $SU(2)$ fusion rules in the spin sector and $SU(3)_2$ fusion rules (listed in Table S2 of the SM [54]) in the orbital sector. This yields multiplets (q, S', λ') , with dimensions d' , energies $E' = E(q, S, \lambda')$, and excitation energies $\delta E' = E' - E'_{\text{min}}$. These are compared to the values, E_{NRG} , computed by NRG for $(J_0, K_0, I_0) = (0, 0.3, 0)$. The NRG energies have been shifted and rescaled such that the lowest energy is zero and the second-lowest values for E_{NRG} and $\delta E'$ match. The single-fusion and NRG spectra agree well (deviations $\lesssim 10\%$). Right: Double fusion, which fuses multiplets from the middle column with an impurity in the conjugate representation $\bar{Q}_{\text{imp}} = (0, 1, \square)$, yields the quantum numbers (q, S'', λ'') . These characterize the CFT boundary operators \hat{O} , with scaling dimensions $\Delta = E(q, S, \lambda'')$.

Free fermions			Single fusion, with $Q_{\text{imp}} = (0, 1, \square)$					NRG	Double fusion, with $\bar{Q}_{\text{imp}} = (0, 1, \square)$							
q	S	λ	d	E	q	S'	λ'	d'	E'	$\delta E'$	E_{NRG}	q	S''	λ''	Δ	\hat{O}
0	0	\bullet	1	0	0	1	\square	9	$\frac{4}{15}$	$\frac{1}{30}$ (0.033)	0.033	0	0	\bullet	0	$\mathbb{1}$
														\square	$\frac{3}{5}$	Φ_{orb}
														\bullet	0	
														\square	$\frac{3}{5}$	
														\bullet	0	
														\square	$\frac{3}{5}$	

Free fermions					Single fusion, with $Q_{\text{imp}} = (0, 1, \square)$						NRG	Double fusion, with $\bar{Q}_{\text{imp}} = (0, 1, \square)$				
q	S	λ	d	E	q	S'	λ'	d'	E'	$\delta E'$	E_{NRG}	q	S''	λ''	Δ	\hat{O}
-2	1	\square	9	1	-2	0	\bullet	1	$\frac{11}{15}$	$\frac{1}{2}$ (0.5)	0.52	-2	1	\square	1	as above, with $S'' \in \{0, 1, 2\}$
							\square	8	$\frac{4}{3}$	$\frac{11}{10}$ (1.1)	1.16			\square	1	
							\bullet	3	$\frac{11}{15}$	$\frac{1}{2}$ (0.5)	0.52			\square	$\frac{7}{5}$	
							\square	24	$\frac{4}{3}$	$\frac{11}{10}$ (1.1)	1.16					
							\bullet	5	$\frac{11}{15}$	$\frac{1}{2}$ (0.5)	0.52					
							\square	40	$\frac{4}{3}$	$\frac{11}{10}$ (1.1)	1.16					
+1	$\frac{3}{2}$	\square	24	$\frac{3}{2}$	+1	$\frac{1}{2}$	\square	16	$\frac{43}{30}$	$\frac{6}{5}$ (1.2)	1.28	+1	$\frac{1}{2}$	\square	$\frac{11}{10}$	as above
							\square	32	$\frac{43}{30}$	$\frac{6}{5}$ (1.2)	1.28			\square	$\frac{11}{10}$	
							\square	48	$\frac{43}{30}$	$\frac{6}{5}$ (1.2)	1.28			\square	$\frac{3}{2}$	
-1	$\frac{3}{2}$	\square	24	$\frac{3}{2}$	-1	$\frac{1}{2}$	\square	6	$\frac{11}{10}$	$\frac{13}{15}$ (0.87)	0.92	-1	$\frac{1}{2}$	\square	$\frac{11}{10}$	as above
							\square	12	$\frac{11}{10}$	$\frac{13}{15}$ (0.87)	0.92			\square	$\frac{11}{10}$	
							\square	18	$\frac{11}{10}$	$\frac{13}{15}$ (0.87)	0.92			\square	$\frac{3}{2}$	
± 3	$\frac{1}{2}$	\square	16	$\frac{3}{2}$	± 3	$\frac{1}{2}$	\square	6	$\frac{7}{6}$	$\frac{14}{15}$ (0.93)	0.98	± 3	$\frac{1}{2}$	\bullet	$\frac{9}{10}$	as above
							\square	12	$\frac{47}{30}$	$\frac{4}{3}$ (1.33)	1.41			\square	$\frac{3}{2}$	
							\square	12	$\frac{7}{6}$	$\frac{14}{15}$ (0.93)	0.98			\bullet	$\frac{9}{10}$	
							\square	24	$\frac{47}{30}$	$\frac{4}{3}$ (1.33)	1.41			\square	$\frac{3}{2}$	
							\square	12	$\frac{7}{6}$	$\frac{14}{15}$ (0.93)	0.98			\square	$\frac{3}{2}$	
							\square	24	$\frac{47}{30}$	$\frac{4}{3}$ (1.33)	1.41			\square	$\frac{3}{2}$	
± 3	$\frac{3}{2}$	\bullet	4	$\frac{3}{2}$	± 3	$\frac{1}{2}$	\square	6	$\frac{53}{30}$	$\frac{23}{15}$ (1.53)	1.63	± 3	$\frac{1}{2}$	\bullet	$\frac{3}{2}$	as above
							\square	12	$\frac{53}{30}$	$\frac{23}{15}$ (1.53)	1.63			\square	$\frac{21}{10}$	
							\square	18	$\frac{53}{30}$	$\frac{23}{15}$ (1.53)	1.63			\bullet	$\frac{3}{2}$	

Having discussed orbital fusion, we now turn to the spin sector—how should the impurity’s spectator spin be dealt with? This question goes beyond the scope of AL’s work, who did not consider impurities with spectator degrees of freedom. We have explored several spin fusion strategies and concluded that the following one yields spectra consistent with NRG: In parallel to orbital fusion, the bath and impurity spin degrees should be combined too, as $S \otimes S_{\text{imp}} = \sum_{\oplus} S'$, but using the

fusion rules of the $SU(2)$ Lie algebra, not the $SU(2)_3$ KM algebra. Heuristically, the difference—KM versus Lie—between the algebras governing orbital and spin fusion reflects the fact that the bath and impurity are *coupled* in the orbital sector, where the bath “absorbs” the impurity orbital isospin, but *decoupled* in the spin sector, where the impurity spin remains a spectator.

The fusion of bath and impurity degrees of freedom, called single fusion by AL, is illustrated schematically in

the left-hand part of Fig. 3 for four selected multiplets. Table II gives a comprehensive list of low-lying multiplets obtained in this manner. On the left it enumerates the 14 lowest-lying multiplets (q, S, λ) of the free bath, with dimensions d and energies $E(q, S, \lambda)$. Fusing these with a $Q_{\text{imp}} = (0, 1, \square)$ impurity yields the multiplets, (q, S', λ') , listed in the center. Their energies are given by $E' = E(q, S, \lambda)$, not $E(q, S', \lambda')$, since at the NFL fixed point, where $J_0 = I_0 = 0$, the impurity spin is decoupled from the bath.

The single-fusion excitation energies, $\delta E' = E' - E'_{\text{min}}$, relative to the lowest-lying multiplet ($E'_{\text{min}} = 7/30$) are in good agreement (deviations $\lesssim 10\%$) with the values, E_{NRG} , found by NRG (for $K_0 = 0.3$, $J_0 = I_0 = 0$) for multiplets with corresponding quantum numbers. The agreement improves upon decreasing the NRG discretization parameter Λ (here $\Lambda = 2.5$ was used). This remarkable agreement between CFT predictions and NRG confirms the applicability of the $SU(2) \otimes SU(3)_2$ fusion hypothesis proposed above.

(C3) As mentioned in Sec. IV, the fixed point $\mathbf{c}_{\text{NFL}}^*$ is characterized by a set of local operators, called boundary operators by AL (since they live at the impurity site, i.e., at the boundary of the two-dimensional space-time on which the CFT is defined). These can be obtained by a second fusion step, called double fusion by AL: the multiplets (q, S', λ') obtained from single fusion are fused with the conjugate impurity representation, $Q_{\text{imp}} = (0, 1, \square)$, to obtain another set of multiplets, (q, S'', λ'') , listed on the right-hand side of Fig. 3 and Table II. (The *conjugate* impurity representation has to be used for double fusion to ensure that the set of boundary operators contains the identity operator, $\bar{\lambda} \otimes \lambda = \mathbb{1}$.) Each such multiplet is associated with a boundary operator \hat{O} with the same quantum numbers and scaling dimension $\Delta = E'' = E(q, S, \lambda'')$. The operators called Φ_{orb} and Φ_{sp} are the leading boundary operators (with smallest scaling dimension) in the orbital and spin sectors, respectively. They determine the behavior of the orbital and spin susceptibilities in the NFL regime (see Sec. VC). In the spin-splitting regime, their role is taken by the operators Ψ_{orb} and Ψ_{sp} , respectively, as discussed in Sec. IV.

C. Scaling behavior of the susceptibilities

In this section, we compute the leading frequency dependence of the dynamical spin and orbital susceptibilities. We begin with the NFL regime, where we directly follow the strategy used by AL in Sec. 3.3 of Ref. [44] and show how it reproduces the results presented in Sec. IV. Thereafter we discuss the SS regime, which has no analog in AL's work, using somewhat more heuristic arguments.

1. NFL regime

At the NFL fixed point, the impurity's orbital isospin \mathbf{T} has been fully absorbed into the bath orbital current \mathcal{J}_{orb} [cf. Eq. (13)]. From this perspective, the impurity orbital susceptibility $\chi_{\text{orb}}^{\text{imp}}$ is governed by the leading local perturbation of the bulk orbital susceptibility, $\chi_{\text{orb}}^{\text{bulk}} \sim \langle \mathcal{J}_{\text{orb}}^{\text{bulk}} | | \mathcal{J}_{\text{orb}}^{\text{bulk}} \rangle_{\omega}$, where $\mathcal{J}_{\text{orb}}^{\text{bulk}}(t) = \int_{-\infty}^{\infty} dx \mathcal{J}_{\text{orb}}(t, x) \sim \mathcal{J}_{\text{orb}, n=0}$ is the bulk orbital current. The leading local perturbations are those combinations of boundary operators (found via double fusion; see Table II) having the smallest scaling dimensions and the same symmetry as the bare Hamiltonian [43–45].

In the orbital sector, the leading boundary operator is Φ_{orb} , with quantum numbers $(0, 0, \square)$ and scaling dimension $\Delta_{\text{orb}} = \frac{3}{5}$ (cf. Tables I and II). The orbital current \mathcal{J}_{orb} has the same quantum numbers. Its first descendant $\mathcal{J}_{\text{orb}, -1}$ can be combined with Φ_{orb} to obtain an orbital $SU(3)$ singlet boundary operator, $H'_{\text{orb}} = \mathcal{J}_{\text{orb}, -1} \cdot \Phi_{\text{orb}}$, with scaling dimension $1 + \Delta_{\text{orb}} = 1 + \frac{3}{5}$. This is the leading irrelevant (dimension > 1) boundary perturbation to the fixed-point Hamiltonian in the orbital sector. Its contribution to the impurity orbital susceptibility, $\chi_{\text{orb}}^{\text{imp}} \sim \chi_{\text{orb}}^{\text{bulk}}$, evaluated perturbatively to second order, is

$$\begin{aligned} \chi_{\text{orb}}^{\text{imp}}(\omega) &\sim \int_{-\infty}^{\infty} dt_1 \int_{-\infty}^{\infty} dt_2 \int_{-\infty}^{\infty} dt_3 e^{i\omega t_1} \\ &\quad \langle \mathcal{J}_{\text{orb}}^{\text{bulk}}(t_1) \cdot \mathcal{J}_{\text{orb}}^{\text{bulk}}(0) H'_{\text{orb}}(t_2) H'_{\text{orb}}(t_3) \rangle \\ &\sim \omega^{2\Delta_{\text{orb}}-1} = \omega^{1/5}. \end{aligned} \quad (14)$$

The last line follows by power counting ($\mathcal{J}_{\text{orb}}^{\text{bulk}}$ has dimension 0, each time integral dimension -1).

The local bath site coupled to the impurity will show the same behavior, $\chi_{\text{orb}}^{\text{bath}} \sim \omega^{1/5}$, since the orbital exchange interaction strongly couples its orbital isospin \mathbf{J}_{orb} to \mathbf{T} —indeed, \mathcal{J}_{orb} is constructed from a linear combination of both these operators [cf. Eq. (13)].

The above results can be obtained in a more direct way by positing that at the NFL fixed point, orbital screening causes both \mathbf{T} and \mathbf{J}_{orb} to be renormalized into the same boundary operator, Φ_{orb} . We then obtain

$$\chi_{\text{orb}}^{\text{imp}}(\omega) \sim \chi_{\text{orb}}^{\text{bath}}(\omega) \sim \langle \Phi_{\text{orb}} | | \Phi_{\text{orb}} \rangle_{\omega} \sim \omega^{2\Delta_{\text{orb}}-1}, \quad (15)$$

reproducing Eq. (14). This is the argument presented in Sec. IV.

We next turn to the spin sector. Exactly at the NFL fixed point, where $J_0 = I_0 = 0$, the impurity spin \mathbf{S} is decoupled from the bath. At $\mathbf{c}_{\text{NFL}}^*$ it hence has no dynamics, scaling dimension 0, and a trivial spin susceptibility, $\chi_{\text{sp}}^{\text{imp}}(\omega) \sim \delta(\omega)$. By contrast, $\chi_{\text{sp}}^{\text{bath}}$, the susceptibility of \mathbf{J}_{sp} , the local bath spin coupled to the impurity, does show nontrivial dynamics at the fixed point. The reason is that some of the boundary operators induced by orbital screening actually live in the spin sector (a highly nontrivial consequence of non-Abelian bosonization and orbital fusion). The leading boundary operator

in the spin sector is Φ_{sp} , with quantum numbers $(0, 1, \bullet)$ and scaling dimension $\Delta_{\text{sp}} = \frac{2}{5}$ (cf. Tables I and II). It can be combined with the first descendant of the (bare, unshifted) spin current to obtain a spin SU(2) singlet boundary operator, $H'_{\text{sp}} = \mathbf{J}_{\text{sp},-1} \cdot \Phi_{\text{sp}}$, with scaling dimension $1 + \Delta_{\text{sp}} = 1 + \frac{2}{5}$. This is the leading irrelevant boundary perturbation to the fixed-point Hamiltonian in the spin sector. Its contribution to the local bath spin susceptibility, $\chi_{\text{sp}}^{\text{bath}} \sim \chi_{\text{sp}}^{\text{bulk}}$, evaluated to second order, is

$$\begin{aligned} \chi_{\text{sp}}^{\text{bath}}(\omega) &\sim \int_{-\infty}^{\infty} dt_1 \int_{-\infty}^{\infty} dt_2 \int_{-\infty}^{\infty} dt_3 e^{i\omega t_1} \\ &\quad \langle \mathbf{J}_{\text{sp}}^{\text{bulk}}(t_1) \cdot \mathbf{J}_{\text{sp}}^{\text{bulk}}(0) H'_{\text{sp}}(t_2) H'_{\text{sp}}(t_3) \rangle \\ &\sim \omega^{2\Delta_{\text{sp}}-1} = \omega^{-1/5}. \end{aligned} \quad (16)$$

This result, too, can be obtained more directly, by positing that \mathbf{J}_{sp} is renormalized to Φ_{sp} , with

$$\chi_{\text{sp}}^{\text{bath}}(\omega) \sim \langle \Phi_{\text{sp}} | | \Phi_{\text{sp}} \rangle_{\omega} \sim \omega^{2\Delta_{\text{sp}}-1}, \quad (17)$$

as argued in Sec. IV.

If the system is tuned very slightly away from the NFL fixed point, $J_0 \ll 1$, $I_0 = 0$, the impurity spin does acquire nontrivial dynamics, due to the action of the spin exchange interaction, $J_0 \mathbf{S} \cdot \mathbf{J}_{\text{sp}}$. According to the above argument, orbital screening renormalizes it to $J_0 \mathbf{S} \cdot \Phi_{\text{sp}}$. Its second-order contribution to the impurity spin susceptibility is

$$\begin{aligned} \chi_{\text{sp}}^{\text{imp}}(\omega) &\sim \int_{-\infty}^{\infty} dt_1 \int_{-\infty}^{\infty} dt_2 \int_{-\infty}^{\infty} dt_3 e^{i\omega t_1} \\ &\quad \langle \mathbf{S}(t_1) \cdot \mathbf{S}(0) (\mathbf{S} \cdot \Phi_{\text{sp}})(t_2) (\mathbf{S} \cdot \Phi_{\text{sp}})(t_3) \rangle \\ &\sim \omega^{2\Delta_{\text{sp}}-3} = \omega^{-11/5}. \end{aligned} \quad (18)$$

The occurrence of such a large, negative exponent for the spin susceptibility is very unusual. It reflects the fact that near (but not at) the NFL fixed point the impurity spin is almost (but not fully) decoupled from the bath, and hence able to “sense” that orbital screening modifies the bath spin current in a nontrivial manner.

2. Spin-splitting regime

The renormalized exchange interaction $J_0 \mathbf{S} \cdot \Phi_{\text{sp}}$ is a relevant perturbation, with scaling dimension $\frac{2}{5} < 1$. It grows under the RG flow, eventually driving the system away from the NFL fixed point and into a crossover regime, $T_{\text{sp}} < \omega < T_{\text{ss}}$, called the spin-splitting regime in Sec. III. In the NRG flow diagram of Fig. 2(a), this regime is characterized by level crossings, extending over several orders of magnitude in energy, rather than a stationary level structure. Hence the SS regime cannot be characterized by proximity to some well-defined fixed point. (A stationary level structure, characteristic of a FL fixed point, emerges only after another crossover, setting in at

the scale T_{sp} .) Nevertheless, Figs. 2(c) and 2(d) show that the local orbital and spin susceptibilities *do* exhibit well-defined power-law behavior in the SS regime:

$$\chi_{\text{orb}}^{\text{imp,bath}}(\omega) \sim \omega^{4/5}, \quad \chi_{\text{sp}}^{\text{imp,bath}}(\omega) \sim \omega^{-6/5}. \quad (19)$$

We define the width of the SS regime as the energy range showing this behavior. It extends over about 3 orders of magnitude, independent of J_0 and I_0 —increasing either of these couplings rigidly shifts the SS regime to larger energies without changing its width (see Fig. 4); i.e., the ratio $T_{\text{sp}}/T_{\text{ss}}$ is independent of these couplings.

The latter fact leads us to conjecture that the NFL fixed point does, after all, govern the SS regime too, though “from afar” rather than from up close. In technical terms, we conjecture that the leading behavior in the SS regime is governed by two different boundary operators, $\tilde{\Psi}_{\text{orb}}$ and $\tilde{\Psi}_{\text{sp}}$, with scaling dimensions $\tilde{\Delta}_{\text{orb}} = \tilde{\Delta}_{\text{sp}} = \frac{9}{10}$ (cf. Tables I and II) instead of the boundary operators Φ_{orb} and Φ_{sp} governing the NFL regime. This conjecture is encoded in the equation above Eq. (10). It states that \mathbf{J}_{orb} and \mathbf{T} are both renormalized to $\tilde{\Psi}_{\text{orb}}$, causing $\chi_{\text{orb}}^{\text{bath}}$ and $\chi_{\text{orb}}^{\text{imp}}$ to scale with the same power,

$$\chi_{\text{orb}}^{\text{bath,imp}} \sim \langle \tilde{\Psi}_{\text{orb}} | | \tilde{\Psi}_{\text{orb}} \rangle_{\omega} \sim \omega^{2\tilde{\Delta}_{\text{orb}}-1} = \omega^{4/5}, \quad (20)$$

and that \mathbf{J}_{sp} and \mathbf{S} are both renormalized to $\mathbf{S} + \tilde{\Psi}_{\text{sp}}$, causing $\chi_{\text{sp}}^{\text{bath}}$ and $\chi_{\text{sp}}^{\text{imp}}$ to scale with the same power,

$$\chi_{\text{sp}}^{\text{bath,imp}} \sim \langle \tilde{\Psi}_{\text{sp}} | | \tilde{\Psi}_{\text{sp}} \rangle_{\omega} \sim \omega^{2\tilde{\Delta}_{\text{sp}}-3} = \omega^{-6/5}. \quad (21)$$

The latter result is obtained in a manner analogous to Eq. (18), with $\mathbf{S} \cdot \Phi$ replaced by $\mathbf{S} \tilde{\Psi}_{\text{sp}}$ [60].

D. Impurity spectral function

We next consider the leading frequency dependence of the impurity spectral function in the NFL regime. For a Kondo-type impurity, this function is given by $-\frac{1}{\pi} \text{Im} \mathcal{T}(\omega)$, where $\mathcal{T}(\omega) = \langle O_{m\sigma} | | O_{m\sigma}^\dagger \rangle_{\omega}$ is the impurity \mathcal{T} matrix, with $O_{m\sigma} = [\psi_{m\sigma}, H_{\text{int}}]$ [63].

As discussed in Sec. VC1, the leading irrelevant boundary operators in the NFL regime are $H'_{\text{orb}} = \mathcal{J}_{\text{orb},-1} \cdot \Phi_{\text{orb}}$ and $H'_{\text{sp}} = \mathbf{J}_{\text{sp},-1} \cdot \Phi_{\text{sp}}$, with scaling dimensions $1 + \Delta_{\text{orb}} = 1 + \frac{3}{5}$ and $1 + \Delta_{\text{sp}} = 1 + \frac{2}{5}$, respectively. AL have shown that a boundary perturbation of this type, with dimension $1 + \Delta$, causes the \mathcal{T} matrix to acquire a leading frequency dependence of $\text{Im} \mathcal{T} \sim |\omega|^\Delta$ [45].

For $\omega > 0$ our NRG results are consistent with $\text{Im} \mathcal{T} \sim \omega^{3/5}$ (cf. Fig. 5). This suggests that the prefactor of H'_{orb} is much larger than that of H'_{sp} , presumably because the computation was done for $J_0 = I_0 = 0$. For $\omega < 0$, by contrast, our numerical results do not exhibit clear power-law behavior for small $|\omega|$, implying that $\text{Im} \mathcal{T}$ does not have particle-hole symmetry. This is

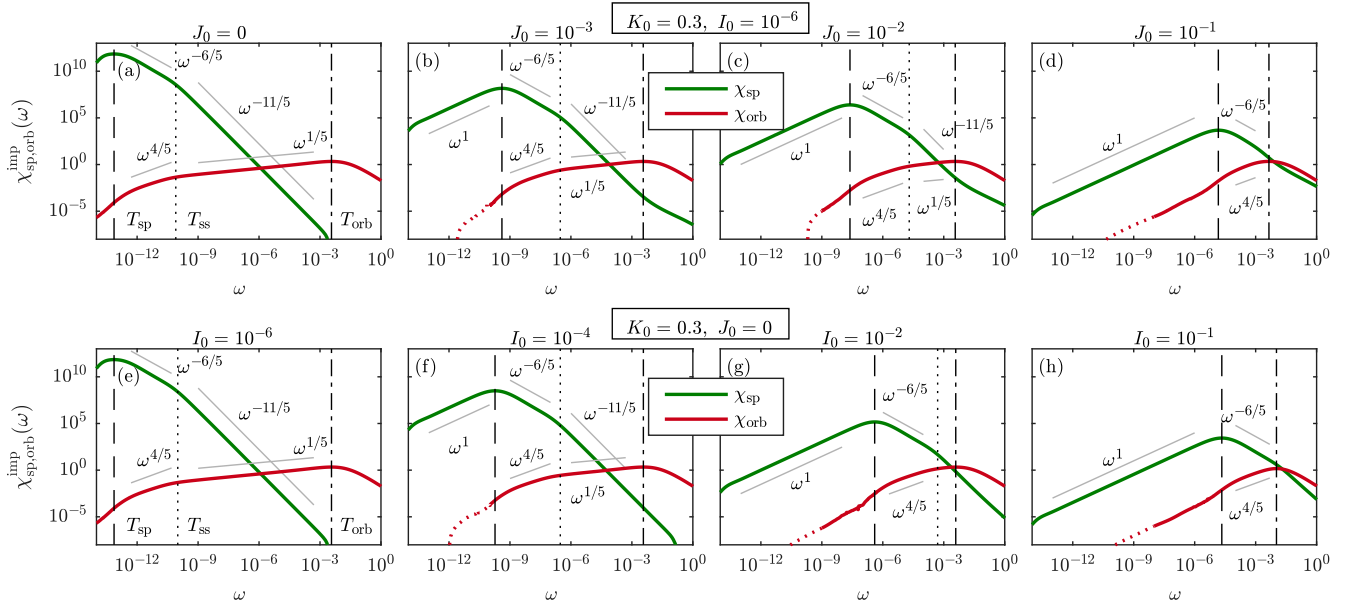


Figure 4. Imaginary part of the zero-temperature impurity spin and orbital susceptibilities for the 3soK model. We keep $K_0 = 0.3$ fixed throughout, and (a)-(d) vary J_0 at fixed $I_0 = 10^{-6}$, or (e)-(h) vary I_0 at fixed $J_0 = 0$. (a)-(d) As J_0 is increased from 0 (left) to 10^{-1} (right), the width of the NFL regime $[T_{\text{ss}}, T_{\text{orb}}]$ shrinks, while that of the SS regime $[T_{\text{sp}}, T_{\text{ss}}]$ remains constant. (e)-(h) We find the same behavior when increasing I_0 with K_0 and J_0 kept fixed.

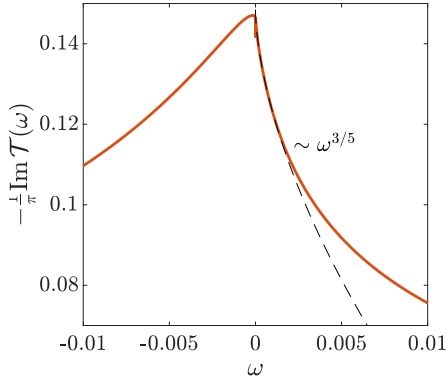


Figure 5. Impurity spectral function, computed by fdm-NRG [52], for $(J_0, K_0, I_0) = (0, 0.3, 0)$. For $\omega > 0$, the $\omega^{3/5}$ behavior is consistent with a boundary perturbation given by H'_{orb} . For $\omega < 0$, clear power law cannot be determined.

not surprising: the 3soK model itself breaks particle-hole symmetry, since under a particle-hole transformation, the impurity’s orbital multiplet \square is mapped to \square . We suspect that the prefactor of the $|\omega|^{\Delta_{\text{orb}}}$ contribution to $\text{Im} \mathcal{T}$ vanishes for $\omega < 0$ for the impurity orbital representation \square , such that only subleading boundary operators, with dimensions $\Delta \geq 9/10$ (cf. Table II), determine the small- ω scaling behavior. However, a detailed understanding of this matter is still lacking.

E. Fermi-liquid fixed point

In this section we show how the FL spectrum at the fixed point \mathbf{c}_{FL}^* can be derived analytically. This can be done in two complementary ways. The first uses $\text{SU}(2)_3$ fusion in the spin sector, the second $\text{SU}(6)_1$ fusion in the flavor (combined spin+orbital) sector.

1. Fermi-liquid spectrum via $\text{SU}(2)_3$ fusion

It is natural to ask whether the FL spectrum at \mathbf{c}_{FL}^* can be derived from the NFL spectrum of $\mathbf{c}_{\text{NFL}}^*$ via some type of fusion in the spin sector, reflecting spin screening induced by the spin exchange interaction. For example, we have tried the following simple strategy (“naive spin fusion”): when setting up the fusion table (Table II), the bath and impurity spin degrees of freedom are combined, $S \otimes S_{\text{imp}} = \sum_{\oplus} S'$, using the fusion rules of the $\text{SU}(2)_3$ KM algebra (Table S3 in the SM [54]) instead of the $\text{SU}(2)$ Lie algebra, and the orbital degrees of freedom, $\lambda \otimes \lambda_{\text{imp}} = \sum_{\oplus} \lambda'$, using $\text{SU}(3)_2$ KM fusion rules (as before; see Table S2 in the SM [54]). Moreover, the energies of the resulting multiplets are computed as $E(q, S', \lambda')$, not $E(q, S, \lambda')$. However, this naive spin fusion strategy completely fails to reproduce the FL fixed point spectrum obtained by NRG, yielding completely different excitation energies and degeneracies.

We suspect that this failure is due to the fact that the RG flow does not directly pass from the NFL regime into the FL regime, but first traverses the intermediate SS

Table III. Fusion table for spin screening at the FL fixed point, \mathbf{c}_{FL}^* , of the 3soK model. It has the same structure as Table II, but here single fusion of bath and impurity multiplets in the charge and spin sectors is performed using $U(1) \times SU(2)_3$ fusion rules (listed in Table S3 of the SM [54]). Moreover, we choose $Q_{\text{imp}} = (1, \frac{3}{2}, \bullet)$ for the impurity, representing the effective local degree of freedom obtained after the completion of orbital screening. The resulting multiplets (q', S', λ) have eigenenergies $E' = E(q', S', \lambda)$ and excitation energies $\delta E' = E' - E'_{\text{min}}$. The NRG energies, computed for $(J_0, K_0, I_0) = (10^{-4}, 0.3, 0)$, have been shifted and rescaled such that the lowest energy is zero and the second-lowest values for E_{NRG} and $\delta E'$ match. The single-fusion and NRG spectra agree very well (deviations $\lesssim 2\%$).

Free fermions					Single fusion, with $Q_{\text{imp}} = (1, \frac{3}{2}, \bullet)$						NRG	Double fusion, with $\bar{Q}_{\text{imp}} = (-1, \frac{3}{2}, \bullet)$			
q	S	λ	d	E	q'	S'	λ'	d	E'	$\delta E'$	E_{NRG}	q''	S''	λ''	Δ
0	0	\bullet	1	0	+1	$\frac{3}{2}$	\bullet	4	$\frac{5}{6}$	$\frac{1}{2}$	0.50	0	0	\bullet	0
+1	$\frac{1}{2}$	\square	6	$\frac{1}{2}$	+2	1	\square	9	1	$\frac{2}{3}$	0.67	+1	$\frac{1}{2}$	\square	$\frac{1}{2}$
-1	$\frac{1}{2}$	\square	6	$\frac{1}{2}$	0	1	\square	9	$\frac{2}{3}$	$\frac{1}{3}$	0.33	-1	$\frac{1}{2}$	\square	$\frac{1}{2}$
0	1	\square	24	1	+1	$\frac{1}{2}$	\square	16	$\frac{5}{6}$	$\frac{1}{2}$	0.50	0	1	\square	1
+2	0	\square	6	1	+3	$\frac{3}{2}$	\square	24	$\frac{13}{6}$	$\frac{11}{6}$	1.87	+2	0	\square	1
-2	0	\square	6	1	-1	$\frac{3}{2}$	\square	24	$\frac{3}{2}$	$\frac{7}{6}$	1.16	-2	0	\square	1
+2	1	\square	9	1	+3	$\frac{1}{2}$	\square	6	$\frac{7}{6}$	$\frac{5}{6}$	0.84	+2	1	\square	1
-2	1	\square	9	1	-1	$\frac{1}{2}$	\square	6	$\frac{1}{2}$	$\frac{1}{6}$	0.17	-2	1	\square	1
+1	$\frac{3}{2}$	\square	24	$\frac{3}{2}$	+2	0	\square	6	1	$\frac{2}{3}$	0.68	+1	$\frac{3}{2}$	\square	$\frac{3}{2}$
-1	$\frac{3}{2}$	\square	24	$\frac{3}{2}$	0	0	\square	6	$\frac{2}{3}$	$\frac{1}{3}$	0.34	-1	$\frac{3}{2}$	\square	$\frac{3}{2}$
± 3	$\frac{1}{2}$	\square	16	$\frac{3}{2}$	-2	1	\square	24	$\frac{4}{3}$	1	0.99	-3	$\frac{1}{2}$	\square	$\frac{3}{2}$
± 3	$\frac{3}{2}$	\bullet	4	$\frac{3}{2}$	-2	0	\bullet	1	$\frac{1}{3}$	0	0.00	-3	$\frac{3}{2}$	\bullet	$\frac{3}{2}$

regime. In the latter, the degeneracy between the two degenerate ground state multiplets of the NFL regime, $(1, \frac{1}{2}, \bullet)$ and $(1, \frac{3}{2}, \bullet)$, is lifted, in a manner that seems to elude a simple description via a modified spin fusion rule.

Instead, the FL spectrum can be obtained via the following arguments. The ground state multiplet of the SS regime, $(1, \frac{3}{2}, \bullet)$, describes an effective local degree of freedom coupled to a bath in such a manner that one bath electron fully screens the impurity orbital isospin, while their spins add to a total spin of $\frac{1}{2} + 1 = \frac{3}{2}$ [see Fig. 2(b)]. Let us view this as an effective impurity with $Q_{\text{imp}} = (1, \frac{3}{2}, \bullet)$. If we combine its charge and spin degrees of freedom with those of a *free* bath, using $q + q_{\text{imp}} = q'$ and $S \oplus S_{\text{imp}} = \sum_{\oplus} S'$, fused according to the $SU(2)_3$ KM algebra, the resulting single-fusion spectrum fully reproduces the FL spectrum found by NRG, as shown in Table III.

2. Fermi-liquid spectrum via $SU(6)_1$ fusion

The FL ground state of the 3soK model is a fully screened spin and orbital singlet. It is therefore natural

to expect that the FL spectrum has a higher symmetry, namely that of the group $U(1) \times SU(6)$, which treats spin and orbital excitations on an equal footing.

This is indeed the case: we now show that the FL spectrum of the 3soK model discussed above matches that of an $SU(6)$ Kondo model which does not distinguish between spin and orbital degrees of freedom. We consider a bath with six flavors of electrons, $H_{\text{bath}} = \sum_p \sum_{\nu=1}^6 \varepsilon_p \psi_{p\nu}^\dagger \psi_{p\nu}$ and an impurity-bath coupling of the form $J_U \mathbf{U} \cdot \mathbf{J}_{\text{fl}}$. Here \mathbf{J}_{fl} is the flavor density at the impurity site, with $J_{\text{fl}}^a = \psi_{\nu}^\dagger \frac{1}{2} \lambda_{\nu\nu'}^a \psi_{\nu'}$, where λ^a are $SU(6)$ matrices in the fundamental representation, and \mathbf{U} describes the impurity's $SU(6)$ flavor isospin, chosen in the fully antisymmetric representation \square . The latter has dimension 15, representing the $\binom{6}{2}$ ways of placing two identical particles into six available states.

Figure 6 shows the NRG finite-size eigenlevel flow for this model. It exhibits a single crossover from a free-impurity fixed point, with ground state multiplet $(q, \lambda) = (0, \square)$, to a FL fixed point, whose ground state multiplet $(-2, \bullet)$ involves complete screening of the impurity's flavor isospin degree of freedom.

This crossover can be described analytically by using non-Abelian bosonization followed by flavor fusion. We

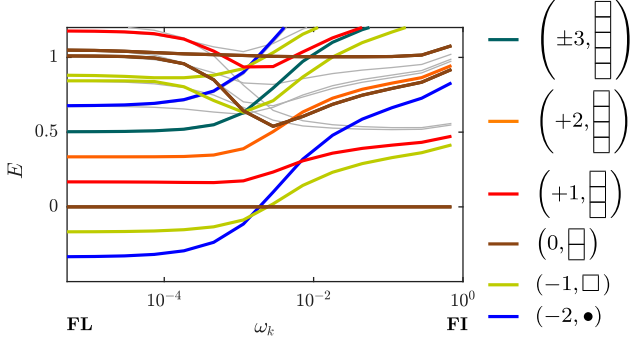


Figure 6. NRG results for the SU(6) Kondo model with $J_U = 0.1$, shown using $\mathcal{E}_{\text{ref}} = \mathcal{E}(0, \square)$ as reference energy. The computation was performed using QSpace [50] to exploit the model's full $U(1) \times SU(6)$ symmetry. (NRG parameters: $\Lambda = 2.5$, $N_{\text{keep}} = 2000$, $D = 1$.)

begin by using non-Abelian bosonization with the $U(1) \times SU(6)_1$ KM current algebra to express the bath excitation spectrum in the form

$$E(q, \lambda) = \frac{1}{12}q^2 + \frac{1}{7}\kappa_6(\lambda) + \ell, \quad (22a)$$

$$\begin{aligned} \kappa_6(\lambda) = & \frac{1}{12}(5\lambda_1^2 + 8\lambda_2^2 + 9\lambda_3^2 + 8\lambda_4^2 + 5\lambda_5^2) \\ & + \frac{1}{2}(5\lambda_1 + 8\lambda_2 + 9\lambda_3 + 8\lambda_4 + 5\lambda_5) \\ & + \frac{1}{6}(6\lambda_2\lambda_3 + 6\lambda_3\lambda_4 + 4\lambda_1\lambda_2 + 4\lambda_2\lambda_4 + 4\lambda_4\lambda_5 \\ & + 3\lambda_1\lambda_3 + 3\lambda_3\lambda_5 + 2\lambda_1\lambda_4 + 2\lambda_2\lambda_5 + \lambda_1\lambda_5) \end{aligned} \quad (22b)$$

with $\ell \in \mathbb{Z}$, where $\kappa_6(\lambda)$ is the quadratic Casimir for the representation $\lambda = (\lambda_1, \lambda_2, \lambda_3, \lambda_4, \lambda_5)$ of the SU(6) Lie algebra [62]. [The contributions from the two terms of Eq. (22a) are listed in Table S4 in the SM [54] for all q and λ values needed in Table IV.] The few lowest-lying (q, λ) multiplets of the free bath, having $E(q, \lambda) \in \frac{1}{2}\mathbb{Z}$, are listed on the left-hand side of Table IV. The strong-coupling FL spectrum can be obtained by combining the bath and impurity flavor degrees of freedom, $\lambda \otimes \lambda_{\text{imp}} = \sum_{\oplus} \lambda'$, using the fusion rules of the $SU(6)_1$ KM algebra (see Table S5 in the SM [54]). The resulting multiplets (q, λ') are listed in the center of Table IV. Their eigenenergies fully match those from NRG.

VI. THREE-ORBITAL ANDERSON-KONDO MODEL

The 3soK model, which we study in detail above, is derived from the more realistic 3oAH model by a Schrieffer-Wolff transformation. In the following, we explore another route for smoothly connecting the physics of the two models, namely starting from the 3oAH model and then additionally turning on the spin and orbital exchange couplings of the 3soK model.

The Hamiltonian of the 3oAH model [22] has the fol-

lowing form: $H_{\text{bath}} + H_{\text{hyb}} + H_{3\text{oAH}}$, where $H_{3\text{oAH}} = \frac{3}{4}J_{\text{H}}N_{\text{imp}} + \frac{1}{2}(U - \frac{1}{2}J_{\text{H}})N_{\text{imp}}(N_{\text{imp}} - 1) - J_{\text{H}}\mathbf{S}^2$, $H_{\text{hyb}} = \sum_{p m \sigma} V_p (f_{m\sigma}^\dagger \psi_{p m \sigma} + \text{H.c.})$, with the impurity occupation $N_{\text{imp}} = \sum_{m\sigma} f_{m\sigma}^\dagger f_{m\sigma}$, where $f_{m\sigma}^\dagger$ creates an impurity electron with spin σ in orbital m . A hybridization function, $\Gamma(\varepsilon) = \pi \sum_p |V_p|^2 \delta(\varepsilon - \varepsilon_p) \equiv \Gamma \Theta(D - |\varepsilon|)$, controls the hopping between the impurity and the bath. U is the local Coulomb interaction and J_{H} the Hund's coupling, favoring a large spin. To this Hamiltonian we add $J_0 \mathbf{S} \cdot \mathbf{J}_{\text{sp}} + K_0 \mathbf{T} \cdot \mathbf{J}_{\text{orb}}$, the Kondo-type spin and orbital exchange couplings between impurity and bath from Eq. (1), with $S^\alpha = f_{m\sigma}^\dagger \frac{1}{2} \sigma_{\sigma\sigma'}^\alpha f_{m\sigma'}$, $T^a = f_{m\sigma}^\dagger \frac{1}{2} \tau_{mm'}^a f_{m'\sigma}$. We treat J_0 and K_0 as free parameters and use them to “deform” the 3oAH model in a way that widens the SOS regime between T_{sp} and T_{orb} .

Free fermions				Single fusion, $Q_{\text{imp}} = (0, \square)$					NRG
q	λ	d	E	q	λ'	d'	E'	$\delta E'$	E_{NRG}
0	●	1	0	0	\square	15	$\frac{2}{3}$	$\frac{1}{3}$	0.33
+1	\square	6	$\frac{1}{2}$	+1	\square	20	$\frac{5}{6}$	$\frac{1}{2}$	0.50
-1	\square	6	$\frac{1}{2}$	-1	\square	6	$\frac{1}{2}$	$\frac{1}{6}$	0.17
+2	\square	15	1	+2	\square	15	1	$\frac{2}{3}$	0.67
-2	\square	15	1	-2	●	1	$\frac{1}{3}$	0	0
± 3	\square	20	$\frac{3}{2}$	± 3	\square	6	$\frac{7}{6}$	$\frac{5}{6}$	0.84

lowing form: $H_{\text{bath}} + H_{\text{hyb}} + H_{3\text{oAH}}$,

$$\begin{aligned} H_{3\text{oAH}} = & \frac{3}{4}J_{\text{H}}N_{\text{imp}} + \frac{1}{2}(U - \frac{1}{2}J_{\text{H}})N_{\text{imp}}(N_{\text{imp}} - 1) - J_{\text{H}}\mathbf{S}^2, \\ H_{\text{hyb}} = & \sum_{p m \sigma} V_p (f_{m\sigma}^\dagger \psi_{p m \sigma} + \text{H.c.}), \end{aligned}$$

with the impurity occupation $N_{\text{imp}} = \sum_{m\sigma} f_{m\sigma}^\dagger f_{m\sigma}$, where $f_{m\sigma}^\dagger$ creates an impurity electron with spin σ in orbital m . A hybridization function, $\Gamma(\varepsilon) = \pi \sum_p |V_p|^2 \delta(\varepsilon - \varepsilon_p) \equiv \Gamma \Theta(D - |\varepsilon|)$, controls the hopping between the impurity and the bath. U is the local Coulomb interaction and J_{H} the Hund's coupling, favoring a large spin. To this Hamiltonian we add $J_0 \mathbf{S} \cdot \mathbf{J}_{\text{sp}} + K_0 \mathbf{T} \cdot \mathbf{J}_{\text{orb}}$, the Kondo-type spin and orbital exchange couplings between impurity and bath from Eq. (1), with $S^\alpha = f_{m\sigma}^\dagger \frac{1}{2} \sigma_{\sigma\sigma'}^\alpha f_{m\sigma'}$, $T^a = f_{m\sigma}^\dagger \frac{1}{2} \tau_{mm'}^a f_{m'\sigma}$. We treat J_0 and K_0 as free parameters and use them to “deform” the 3oAH model in a way that widens the SOS regime between T_{sp} and T_{orb} .

Figures 7(a)-7(d) show how the spin and orbital susceptibilities change upon increasing $|J_0|$ and $|K_0|$, with $J_0 < 0$ and $K_0 > 0$. A pure 3oAH model, with $(J_0, K_0) =$

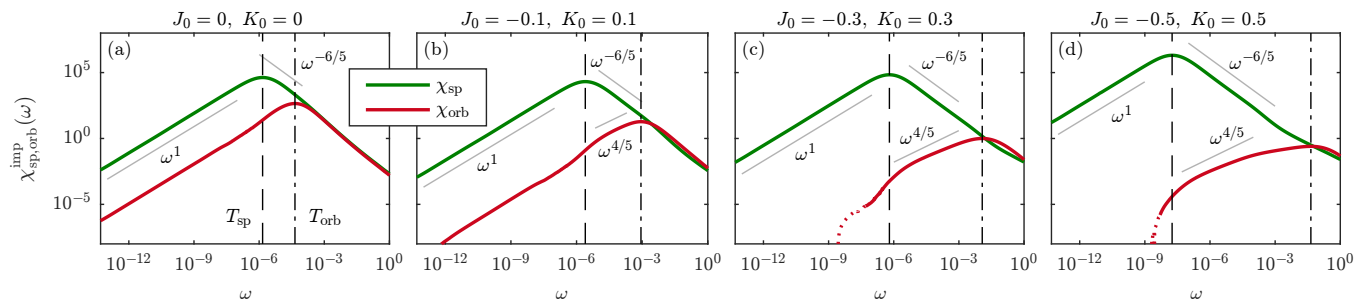


Figure 7. Imaginary part of the impurity spin and orbital susceptibilities for the Anderson-Kondo model, with $U = 5$, $J_H = 1$, $\Gamma = 0.1$, $I_0 = 0$, and J_0, K_0 varying from (a) $J_0 = K_0 = 0$ (pure Anderson-Hund model) to (d) $-J_0 = K_0 = 0.5$. The energy scales for spin and orbital screening, T_{sp} and T_{orb} are pushed apart with increasing $-J_0 = K_0$.

(0,0), clearly shows spin-orbital separation, but T_{sp} and T_{orb} differ by less than two decades [Fig. 7(a); see also Ref. [22]]. Though the SOS window is too small to reveal a true power law for $\chi_{\text{sp}}^{\text{imp}}$, the hints of $\omega^{-6/5}$ behavior are already discernable. Turning on the additional exchange coupling terms, with $J_0 < 0$ and $K_0 > 0$, causes T_{sp} to decrease and T_{orb} to increase, respectively, widening the SOS regime [Figs. 7(b)-7(d)]. For $(J_0, K_0) = (-0.5, 0.5)$ it spans more than 6 orders of magnitude, so that clear power laws, $\chi_{\text{sp}}^{\text{imp}} \sim \omega^{-6/5}$ and $\chi_{\text{orb}}^{\text{imp}} \sim \omega^{4/5}$, become accessible [Fig. 7(d)]. These power laws are consistent with our findings for the spin-splitting regime in Secs. III and V. This scenario is evidently smoothly connected to that of the pure 3soK model [Fig. 2(c)]. There the absence of charge fluctuations makes it possible to fully turn off the I_0 contribution implicitly present in the 3oAH model, thereby widening the SOS regime even further and allowing the true NFL regime to be analyzed in detail.

VII. CONCLUSION

While the main aim of this work was to understand NFL behavior in Hund metals, it has much wider implications, as already indicated in Sec. I. Let us assess these from several perspectives of increasing generality.

(i) We have used NRG and CFT to elucidate the NFL regime of a 3soK model, fine-tuned such that spin screening sets in at very much lower energies than orbital screening. We were able to analytically compute the scaling behavior of dynamical spin and orbital susceptibilities, finding $\chi_{\text{orb}}^{\text{imp}} \sim \omega^{1/5}$, $\chi_{\text{sp}}^{\text{imp}} \sim \omega^{-11/5}$ in the NFL regime and $\chi_{\text{sp}}^{\text{imp}} \sim \omega^{-6/5}$ in the spin-splitting regime. The main significance of these findings lies in the qualitative physical behavior which they imply. An orbital susceptibility decreasing with an exponent < 1 , rather than the Fermi-liquid exponent 1, indicates that the orbital degrees of freedom, though screened, are still affected by the unscreened spin degrees of freedom. A spin susceptibility diverging as $\omega^{-\gamma}$, with $\gamma > 1$, indicates anomalously strong spin fluctuations. This seems to be a characteristic property of the incoherent regime of Hund

metals. As pointed out in Sec. I, anomalously strong spin fluctuations have direct consequences for theories of the superconducting state of the iron pnictides [14].

(ii) We have uncovered the origin of hints of NFL behavior found previously for a 3oAH model and related models [1, 3-5, 8, 22-24]. There the spin-orbital coupling I_0 is always nonzero, preventing RG trajectories from closely approaching the NFL fixed point. Nevertheless, even if they pass this fixed point “at a distance,” it still leaves traces of NFL behavior for various observables, such as $\chi_{\text{sp}}^{\text{imp}} \sim \omega^{-6/5}$ behavior for the imaginary part of the impurity’s dynamical spin susceptibility. We showed in Sec. VI how NFL behavior emerges if the 3oAH model is “deformed” by additionally turning on the spin and orbital exchange couplings of the 3soK model, thereby adiabatically connecting the SS regime of the 3soK model to the incoherent regime of the 3oAH model. Furthermore, it has been shown in Ref. [22] that DMFT self-consistency does not significantly influence the behavior of the susceptibilities in the 3oAH model. Thus our conclusions, in particular regarding the prevalence of strong spin fluctuations in the SOS regime, should also apply to DMFT calculations. Indeed, DMFT studies [22, 47] of a self-consistent 3oAH model contain results for $\chi_{\text{sp}}^{\text{imp}}$ which, in the SOS window, are consistent with the $\omega^{-6/5}$ scaling found and explained here for the SS regime.

(iii) Taking a broader perspective, we have provided an analytic solution of a paradigmatic example of a “Hund impurity problem.” We were able to address this fundamental type of problem by combining state-of-the-art multiorbital NRG with a suitable generalization of Affleck and Ludwig’s CFT approach [42-46].

(iv) Regarding experimental relevance, Hund impurities are of central importance for understanding Hund metals, including almost all $4d$ and $5d$ materials, and even in the $5f$ actinides Hund’s coupling is the main cause for electronic correlations. Our work illustrates paradigmatically why hints of NFL physics can generically be expected to arise in such systems. Moreover, *tunable* Hund impurities can be realized using magnetic molecules on substrates [64] or multilevel quantum dots, raising hopes of tuning Hund impurities in such a way that truly well-developed NFL behavior can be observed

experimentally.

ACKNOWLEDGMENTS

We thank I. Affleck, A. Georges, M. Goldstein, O. Parcollet, E. Sela and A. Tsvelik for helpful advice and, in particular, I. Brunner for technical advice regarding $SU(3)_2$ fusion rules. E. W., K. M. S., and J. v. D. are supported by the Deutsche Forschungsgemeinschaft under Germany’s Excellence Strategy—EXC-2111—390814868, and S.-S. B. L. by Grant No. LE3883/2-1. A. W. was supported by the U.S. Department of Energy, Office of Basic Energy Sciences, under Contract No. DE-SC0012704. G. K. was supported by the National Science Foundation Grant No. DMR-1733071. Y. W. was supported by the U.S. Department of Energy, Office of Science, Basic Energy Sciences as a part of the Computational Materials Science Program through the Center for Computational Design of Functional Strongly Correlated Materials and Theoretical Spectroscopy.

Note added.—Recently, a paper closely related to ours appeared [65], with similar goals, a complementary analysis (using NRG but not CFT), and conclusions consistent with ours.

Appendix: Ye’s $SU(2) \times SU(2)$ spin-orbital Kondo model

In this appendix, we revisit an $SU(2) \times SU(2)$ spin-orbital Kondo (2soK) model studied in a pioneering paper by Ye in 1997 [48]. It is a simpler cousin of our 3soK model, having a Hamiltonian of precisely the same form, with the following differences: the orbital channel index takes only two values, $m = 1, 2$; the local orbital current \mathbf{J}_{orb} is defined using Pauli (not Gell-Mann) matrices; and the impurity spin and orbital isospin operators, \mathbf{S} and \mathbf{T} , are both $SU(2)$ generators, in the representation $S = \lambda = \frac{1}{2}$.

In the context of the present study, Ye’s paper is of interest because his Kondo impurity likewise features both spin and orbital degrees of freedom. From a conceptual perspective, his and our models differ only in the symmetry group, $SU(2)$ versus $SU(3)$ in the orbital sector, and the choice of impurity multiplet, $Q_{\text{imp}} = (\frac{1}{2}, \frac{1}{2})$ versus $(1, \square)$. Moreover, he was able to obtain exact results for his model using Abelian bosonization. Below, we verify that when the NRG and CFT methodology used in the main text is applied to Ye’s 2soK model, the results are consistent with his conclusions.

Before proceeding, however, let us also briefly address some differences between Ye’s work and ours. Since he

We have also computed the imaginary parts of spin and orbital susceptibilities $\chi_{\text{sp,orb}}^{\text{imp}}(\omega)$. Figure 8(b) shows the results. Both functions approach constants in the zero-frequency limit, i.e., scale as ω^0 . This can be understood

uses Abelian bosonization, his approach does not readily generalize to the $U(1) \times SU(2) \times SU(3)$ impurity model considered here. Ye does mention very briefly that some of his results can also be obtained using non-Abelian bosonization, employing *simultaneous* fusion in the spin and orbital sectors. However, we show below that that fusion scheme is applicable only when particle-hole symmetry is present. This is the case for Ye’s application, but not for our 3soK model. When particle-hole symmetry is absent, the fusion schemes needed for the spin and orbital are subtly different—indeed, clarifying these differences was the conceptually most challenging aspect of our work. Note that the particle-hole asymmetry of our 3soK model is not a mere technical complication, but an essential ingredient of the physics of Hund metals, which typically feature fillings one particle away from half filling. Finally, note that Ye’s model, involving an impurity with spin $1/2$, is not relevant for Hund metals, where Hund’s coupling favors local spins larger than $1/2$.

1. $I_0 = 0$: NFL fixed point

For $I_0 = 0$, the 2soK model obeys particle-hole symmetry. Figure 8(a) shows the finite-size eigenlevel flow computed by NRG for $\mathbf{c}_0 = (J_0, K_0, I_0) = (0.1, 0.3, 0)$. The low-energy fixed-point spectrum features equidistant levels, but nevertheless has NFL properties, as predicted by Ye, in that it cannot be understood in terms of combinations of single-particle excitations. Remarkably, this fixed-point spectrum can be reproduced by CFT arguments. Using non-Abelian bosonization according to the $U(1) \times SU(2)_2 \times SU(2)_2$ KM algebra, the spectrum of free bath excitations can be expressed as

$$E(q, S, \lambda) = \frac{1}{8}q^2 + \frac{1}{4}\kappa_2(S) + \frac{1}{4}\kappa_2(\lambda) + \ell, \quad (\text{A1a})$$

$$\kappa_2(S) = S(S+1), \quad \kappa_2(\lambda) = \lambda(\lambda+1), \quad (\text{A1b})$$

with $\ell \in \mathbb{Z}$, while $\kappa_2(S)$, $\kappa_2(\lambda)$ are the quadratic $SU(2)$ Casimirs in the spin and orbital sectors, respectively. We now combine bath and impurity degrees of freedom using *simultaneous* fusion in the spin and orbital sectors, $S \otimes S_{\text{imp}} = \sum_{\oplus} S'$ and $\lambda \otimes \lambda_{\text{imp}} = \sum_{\oplus} \lambda'$, employing the fusion rules of the $SU(2)_2 \times SU(2)_2$ KM algebra (Table S7 in the SM [54]). This reproduces the NFL fixed-point spectrum found by NRG, as shown in Table V.

By contrast, we recall that for the 3soK model our attempts to use simultaneous spin and orbital fusion to obtain the FL ground state for $0 \neq J_0 \ll K_0$, $I_0 = 0$, were unsuccessful (cf. Sec. VE1). Thus the 2soK and 3soK models provide an example and a counterexample for the success of simultaneous spin and orbital fusion, succeeding or failing for a NFL or FL fixed point spectrum, respectively.

in terms of the scaling dimensions of the leading boundary operators in the spin and orbital sectors, Φ_{sp} and Φ_{orb} , which have dimensions $\Delta_{\text{sp}} = \Delta_{\text{orb}} = \frac{1}{2}$ (Table V).

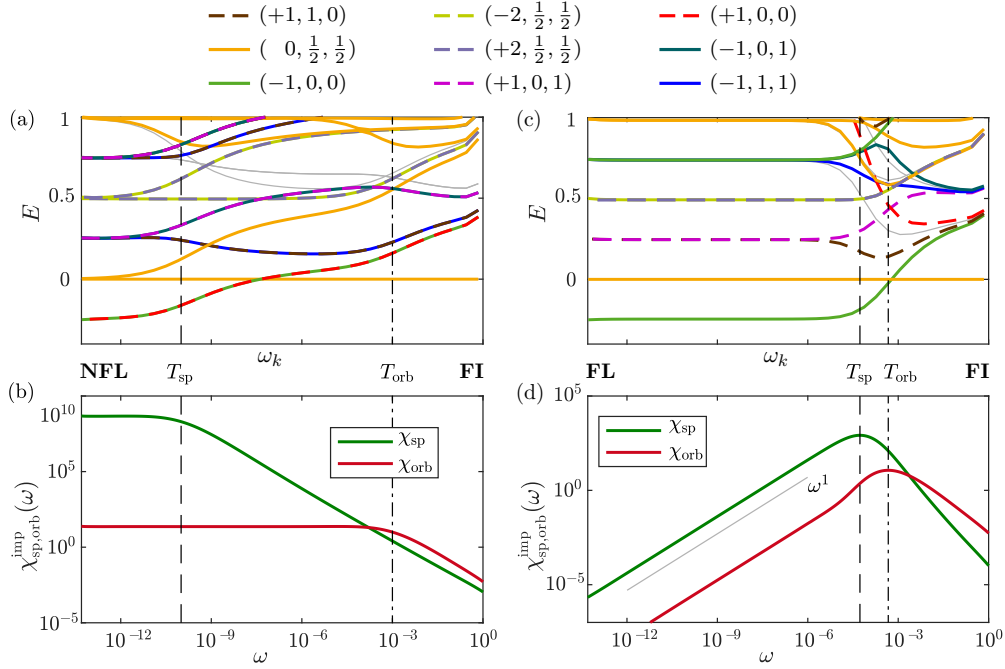


Figure 8. NRG results for Ye's 2soK model, computed (a,b) for $(J_0, K_0, I_0) = (0.1, 0.3, 0)$, respecting particle-hole symmetry, and (c,d) for $(0, 0.3, 0.05)$, breaking particle-hole symmetry. (a,c) Eigenlevel flow diagrams, with quantum numbers (q, S, λ) shown at the top. The low-energy fixed points in (a) and (c) exhibit a NFL or FL spectrum, respectively, reproduced analytically in Table V or VI, respectively. (b,d) Imaginary part of the impurity's spin and orbital susceptibilities. Vertical lines indicate the crossover scales for orbital screening, T_{orb} (dash-dotted) and spin screening, T_{sp} (dashed), marking when χ_{orb}^{imp} and χ_{sp}^{imp} (b) bend over to constant behavior, or (d) reach their maxima, respectively. (NRG parameters: $\Lambda = 2.5$, $N_{keep} = 2000$, $D = 1$.)

By the arguments of Sec. VC, we thus obtain

$$\chi_{sp,orb}^{imp} \sim \omega^{2\Delta_{sp,orb}-1} \sim \omega^0,$$

as predicted by Ye. This resembles the behavior observed for the celebrated two-channel Kondo model, featuring a spin-1/2 impurity having no orbital isospin (obtained from Ye's model by using $\lambda = \bullet$ for the impurity orbital pseudospin, and setting $K_0 = I_0 = 0$).

2. $I_0 \neq 0$: FL fixed point

For $I_0 \neq 0$, particle-hole symmetry is broken. Figure 8(c) shows the eigenlevel flow computed by NRG for $\mathbf{c}_0 = (0, 0.3, 0.05)$. The low-energy fixed point is a FL, as predicted by Ye. Its spectrum shows the same equidistant set of energies as the NFL spectrum of $I_0 = 0$ [Fig. 8(a)], but the degeneracies are different. This fixed point *cannot* be understood by simultaneous fusion in the spin and orbital sector. However, it agrees with the FL spectrum of an SU(4) Kondo model with the higher symmetry $U(1)_{ch} \times SU(4)_f$, defined in analogy to the SU(6) Kondo model from Sec. VE2, with a flavor index $\nu = 1, \dots, 4$ encoding both spin and orbital degrees of freedom. Using non-Abelian bosonization according to the $U(1) \times SU(4)_1$ KM algebra, the free bath spectrum can be expressed as

$$E(q, \lambda) = \frac{1}{8}q^2 + \frac{1}{5}\kappa_4(\lambda) + \ell, \quad (\text{A2a})$$

$$\kappa_4(\lambda) = \frac{1}{8}(3\lambda_1^2 + 4\lambda_2^2 + 3\lambda_3^2 + 4\lambda_1\lambda_2 + 2\lambda_2\lambda_3 + 4\lambda_1\lambda_3 + 12\lambda_1 + 16\lambda_2 + 12\lambda_3). \quad (\text{A2b})$$

with $\ell \in \mathbb{Z}$, where $\kappa_4(\lambda)$ is the quadratic Casimir for the $\lambda = (\lambda_1, \lambda_2, \lambda_3)$ representation of the SU(4) Lie algebra. [The contributions from the two terms of Eq. (A2a) are listed in Table S8 of the Supplemental Material [54] for the lowest few q and λ values.] Combining the flavor degrees of freedom of bath and impurity, $\lambda \otimes \lambda_{imp} = \sum_{\oplus} \lambda'$, using the fusion rules of the $SU(4)_1$ KM algebra, we recover the FL fixed point spectrum found by NRG. This is shown in Table VI. In the FL regime, the spin and orbital susceptibilities scale as $\chi_{sp,orb}^{imp} \sim \omega^1$ [Fig. 8(d)], as expected for a Fermi liquid and predicted by Ye.

Table V. Fusion table for the NFL fixed point of Ye's 2soK model. It is structured just as Table II for the 3soK model, but here the free bath excitations are computed using Eqs. (A1) and Table S6 of the SM [54], and single fusion of bath and impurity degrees of freedom is performed simultaneously in the spin and orbital sectors, using $SU(2)_2 \times SU(2)_2$ fusion rules (listed in Table S7 of the SM [54]). The resulting multiplets (q, S', λ') have energies $E' = E(q, S', \lambda')$ and excitation energies $\delta E' = E' - E'_{\min}$. The NRG energies, computed for $(J_0, K_0, I_0) = (0.1, 0.3, 0)$ [Fig. 8(a)] have been shifted and rescaled such that the lowest energy is zero and the second-lowest values for E_{NRG} and $\delta E'$ match. The single-fusion and NRG spectra agree very well (deviations $\lesssim 1\%$).

Free fermions					Single fusion, with $Q_{\text{imp}} = (0, \frac{1}{2}, \frac{1}{2})$						NRG	Double fusion, with $Q_{\text{imp}} = (0, \frac{1}{2}, \frac{1}{2})$					
q	S	λ	d	E	q	S'	λ'	d'	E'	$\delta E'$	E_{NRG}	q	S''	λ''	Δ	\hat{O}	
0	0	0	1	0	0	$\frac{1}{2}$	$\frac{1}{2}$	4	$\frac{3}{8}$	$\frac{1}{4}$	0.25	0	$\left\{ \begin{array}{l} 0 \\ 1 \end{array} \right.$	$\left\{ \begin{array}{l} 0 \\ 1 \\ 0 \\ 1 \end{array} \right.$	$\frac{0}{\frac{1}{2}}$ $\frac{1}{\frac{1}{2}}$	Φ_{orb} Φ_{sp}	
± 1	$\frac{1}{2}$	$\frac{1}{2}$	4	$\frac{1}{2}$	± 1	$\left\{ \begin{array}{l} 0 \\ 1 \end{array} \right.$	$\left\{ \begin{array}{l} 0 \\ 1 \end{array} \right.$	1	$\frac{1}{8}$	0	0						
										3	$\frac{5}{8}$	$\frac{1}{2}$	0.5				
								3	$\frac{5}{8}$	$\frac{1}{2}$	0.5						
								9	$\frac{9}{8}$	1	0.99						
0	1	0	3	$\frac{1}{2}$	0	$\frac{1}{2}$	$\frac{1}{2}$	4	$\frac{3}{8}$	$\frac{1}{4}$	0.25						
0	0	1	3	$\frac{1}{2}$	0	$\frac{1}{2}$	$\frac{1}{2}$	4	$\frac{3}{8}$	$\frac{1}{4}$	0.25						
± 2	0	0	1	$\frac{1}{2}$	± 2	$\frac{1}{2}$	$\frac{1}{2}$	4	$\frac{7}{8}$	$\frac{3}{4}$	0.75						
± 2	1	0	1	1	± 2	$\frac{1}{2}$	$\frac{1}{2}$	4	$\frac{7}{8}$	$\frac{3}{4}$	0.75						
± 2	0	1	1	1	± 2	$\frac{1}{2}$	$\frac{1}{2}$	4	$\frac{7}{8}$	$\frac{3}{4}$	0.75						
± 2	1	1	1	$\frac{3}{2}$	± 2	$\frac{1}{2}$	$\frac{1}{2}$	4	$\frac{7}{8}$	$\frac{3}{4}$	0.75						

Table VI. Fusion table for the FL fixed point of the $SU(4)$ Kondo model. It is structured just as Table IV for the $SU(6)$ Kondo model, but here the free bath excitations are computed using Eqs. (A2) and Table S8 of the SM [54], and flavor fusion is performed using $SU(4)_1$ fusion rules (Table S9 of the SM[54]). The NRG spectrum was computed for the 2soK model with $(J_0, K_0, I_0) = (0, 0.3, 0.05)$ [Fig. 8(c)]. The single-fusion and NRG spectra agree very well (deviations $\lesssim 1\%$).

Free fermions				Single fusion, $Q_{\text{imp}} = (0, \square)$					NRG
q	λ	d	E	q	λ'	d'	E'	$\delta E'$	E_{NRG}
0	\bullet	1	0	0	\square	4	$\frac{3}{8}$	$\frac{1}{4}$	0.25
+1	\square	4	$\frac{1}{2}$	+1	\square	6	$\frac{5}{8}$	$\frac{1}{2}$	0.50
-1	\square	4	$\frac{1}{2}$	-1	\bullet	1	$\frac{1}{8}$	0	0
± 2	\square	6	1	± 2	\square	4	$\frac{7}{8}$	$\frac{3}{4}$	0.75
+3	\square	4	$\frac{3}{2}$	+3	\bullet	1	$\frac{9}{8}$	1	1.00
-3	\square	4	$\frac{3}{2}$	-3	\square	6	$\frac{13}{8}$	$\frac{3}{2}$	1.50

- [1] A. Georges, L. de' Medici, and J. Mravlje, "Strong electronic correlations from Hund's coupling," *Annu. Rev. Condens. Matter Phys.* **4**, 137 (2013).
- [2] P. Werner, E. Gull, M. Troyer, and A. J. Millis, "Spin freezing transition and non-Fermi-liquid self-energy in a three-orbital model," *Phys. Rev. Lett.* **101**, 16 (2008).
- [3] K. Haule and G. Kotliar, "Coherence-incoherence crossover in the normal state of iron oxypnictides and importance of Hund's rule coupling," *New J. Phys.* **11**, 025021 (2009).
- [4] Z. P. Yin, K. Haule, and G. Kotliar, "Magnetism and charge dynamics in iron pnictides," *Nat. Phys.* **7**, 294 (2011).
- [5] Z. P. Yin, K. Haule, and G. Kotliar, "Kinetic frustration and the nature of the magnetic and paramagnetic states in iron pnictides and iron chalcogenides," *Nat. Mater.* **10**, 932 (2011).
- [6] L. de' Medici, J. Mravlje, and A. Georges, "Janus-faced influence of Hund's rule coupling in strongly correlated materials," *Phys. Rev. Lett.* **107**, 25 (2011).
- [7] J. Mravlje, M. Aichhorn, T. Miyake, K. Haule, G. Kotliar, and A. Georges, "Coherence-incoherence crossover and the mass-renormalization puzzles in Sr_2RuO_4 ," *Phys. Rev. Lett.* **106**, 9 (2011).
- [8] Z. P. Yin, K. Haule, and G. Kotliar, "Fractional power-law behavior and its origin in iron-chalcogenide and ruthenate superconductors: Insights from first-principles calculations," *Phys. Rev. B* **86**, 195141 (2012).
- [9] C. Aron and G. Kotliar, "Analytic theory of Hund's metals: A renormalization group perspective," *Phys. Rev. B* **91**, 041110 (2015).
- [10] S. Hoshino and P. Werner, "Superconductivity from emerging magnetic moments," *Phys. Rev. Lett.* **115**, 247001 (2015).
- [11] H. T. Dang, J. Mravlje, A. Georges, and A. J. Millis, "Electronic correlations, magnetism, and Hund's rule coupling in the ruthenium perovskites SrRuO_3 and CaRuO_3 ," *Phys. Rev. B* **91**, 195149 (2015).
- [12] J. Mravlje and A. Georges, "Thermopower and entropy: Lessons from Sr_2RuO_4 ," *Phys. Rev. Lett.* **117**, 036401 (2016).
- [13] M. Zingl, J. Mravlje, M. Aichhorn, O. Parcollet, and A. Georges, "Hall coefficient signals orbital differentiation in the Hund's metal Sr_2RuO_4 ," *npj Quantum Mater.* **4**, 35 (2019).
- [14] T.-H. Lee, A. Chubukov, H. Miao, and G. Kotliar, "Pairing mechanism in Hund's metal superconductors and the universality of the superconducting gap to critical temperature ratio," *Phys. Rev. Lett.* **121**, 187003 (2018).
- [15] M. Yi, D. H. Lu, R. Yu, S. C. Riggs, J.-H. Chu, B. Lv, Z. K. Liu, M. Lu, Y.-T. Cui, M. Hashimoto, S.-K. Mo, Z. Hussain, C. W. Chu, I. R. Fisher, Q. Si, and Z.-X. Shen, "Observation of temperature-induced crossover to an orbital-selective Mott phase in $\text{A}_x\text{Fe}_{2-y}\text{Se}_2$ ($\text{A}=\text{K}, \text{Rb}$) superconductors," *Phys. Rev. Lett.* **110**, 067003 (2013).
- [16] F. Hardy, A. E. Böhmer, D. Aoki, P. Burger, T. Wolf, P. Schweiss, R. Heid, P. Adelman, Y. X. Yao, G. Kotliar, J. Schmalian, and C. Meingast, "Evidence of strong correlations and coherence-incoherence crossover in the iron pnictide superconductor $\text{KF}_{e_2}\text{As}_2$," *Phys. Rev. Lett.* **111**, 027002 (2013).
- [17] A. Horvat, R. Žitko, and J. Mravlje, "Low-energy physics of three-orbital impurity model with Kanamori interaction," *Phys. Rev. B* **94**, 165140 (2016).
- [18] A. Tamai, M. Zingl, E. Rozbicki, E. Cappelli, S. Riccò, A. de la Torre, S. McKeown Walker, F. Y. Bruno, P. D. C. King, W. Meevasana, M. Shi, M. Radović, N. C. Plumb, A. S. Gibbs, A. P. Mackenzie, C. Berthod, H. U. R. Strand, M. Kim, A. Georges, and F. Baumberger, "High-resolution photoemission on Sr_2RuO_4 reveals correlation-enhanced effective spin-orbit coupling and dominantly local self-energies," *Phys. Rev. X* **9**, 021048 (2019).
- [19] P. Werner and S. Hoshino, "Nickelate superconductors – multiorbital nature and spin freezing," (2019), [arXiv:1910.00473 \[cond-mat.str-el\]](https://arxiv.org/abs/1910.00473).
- [20] P. Coleman, Y. Komijani, and E. König, "The triplet resonating valence bond state and superconductivity in Hund's metals," (2019), [arXiv:1910.03168 \[cond-mat.str-el\]](https://arxiv.org/abs/1910.03168).
- [21] X. Chen, I. Krivenko, M. B. Stone, A. I. Kolesnikov, T. Wolf, D. Reznik, K. S. Bedell, F. Lechermann, and S. D. Wilson, "Unconventional Hund metal in MnSi ," (2019), [arXiv:1909.11195 \[cond-mat.str-el\]](https://arxiv.org/abs/1909.11195).
- [22] K. M. Stadler, Z. P. Yin, J. von Delft, G. Kotliar, and A. Weichselbaum, "Dynamical mean-field theory plus numerical renormalization-group study of spin-orbital separation in a three-band Hund metal," *Phys. Rev. Lett.* **115**, 136401 (2015).
- [23] K. M. Stadler, G. Kotliar, A. Weichselbaum, and J. von Delft, "Hundness versus Mottness in a three-band Hubbard-Hund model: On the origin of strong correlations in Hund metals," *Ann. Phys.* **405**, 365 (2018).
- [24] X. Deng, K. M. Stadler, K. Haule, A. Weichselbaum, J. von Delft, and G. Kotliar, "Signatures of Mottness and Hundness in archetypal correlated metals," *Nat. Commun.* **10**, 2721 (2019).
- [25] S. Akhanjee and A. M. Tsvelik, "Analytically tractable model of bad metals," *Phys. Rev. B* **87**, 195137 (2013).
- [26] J. Kondo, "Resistance minimum in dilute magnetic alloys," *Prog. Theor. Phys.* **32**, 37 (1964).
- [27] P. W. Anderson, "A poor man's derivation of scaling laws for the Kondo problem," *J. Phys. C* **3**, 2436 (1970).
- [28] K. G. Wilson, "The renormalization group: Critical phenomena and the Kondo problem," *Rev. Mod. Phys.* **47**, 773 (1975).
- [29] J. R. Schrieffer, "The Kondo effect—the link between magnetic and nonmagnetic impurities in metals?" *J. Appl. Phys.* **38**, 1143 (1967).
- [30] M. D. Daybell and W. A. Steyert, "Localized magnetic impurity states in metals: Some experimental relationships," *Rev. Mod. Phys.* **40**, 380 (1968).
- [31] B. Coqblin and J. R. Schrieffer, "Exchange interaction in alloys with cerium impurities," *Phys. Rev.* **185**, 847 (1969).
- [32] I. Okada and K. Yosida, "Singlet ground state of the localized d-electrons coupled with conduction electrons in metals," *Prog. Theor. Phys.* **49**, 1483 (1973).
- [33] Ph. Nozières and A. Blandin, "Kondo effect in real metals," *Journal de Physique* **41**, 193 (1980).
- [34] N. Andrei and C. Destri, "Solution of the multichannel Kondo problem," *Phys. Rev. Lett.* **52**, 364 (1984).

- [35] A. M. Tsvelik and P. B. Wiegmann, “Solution of the n -channel Kondo problem (scaling and integrability),” *Z. Phys. B* **54**, 201 (1984).
- [36] A. M. Tsvelik, “The thermodynamics of multichannel Kondo problem,” *J. Phys. C: Solid St. Phys.* **18**, 159 (1985).
- [37] A. M. Tsvelik and P. B. Wiegmann, “Exact solution of the multichannel Kondo problem, scaling, and integrability,” *J. Stat. Phys.* **38**, 125 (1985).
- [38] N. Andrei and A. Jerez, “Fermi- and non-Fermi-liquid behavior in the anisotropic multichannel Kondo model: Bethe ansatz solution,” *Phys. Rev. Lett.* **74**, 4507 (1995).
- [39] A. Jerez, N. Andrei, and G. Zaránd, “Solution of the multichannel Coqblin-Schrieffer impurity model and application to multilevel systems,” *Phys. Rev. B* **58**, 3814 (1998).
- [40] D. M. Cragg, P. Lloyd, and P. Nozieres, “On the ground states of some s-d exchange Kondo Hamiltonians,” *J. Phys. C: Solid State Phys.* **13**, 803–817 (1980).
- [41] H. B. Pang and D. L. Cox, “Stability of the fixed point of the two-channel Kondo Hamiltonian,” *Phys. Rev. B* **44**, 9454–9457 (1991).
- [42] I. Affleck, “A current algebra approach to the Kondo effect,” *Nucl. Phys. B* **336**, 517 (1990).
- [43] I. Affleck and A. W. W. Ludwig, “The Kondo effect, conformal field theory and fusion rules,” *Nucl. Phys. B* **352**, 849 (1991).
- [44] I. Affleck and A. W. W. Ludwig, “Critical theory of overscreened Kondo fixed points,” *Nucl. Phys. B* **360**, 641 (1991).
- [45] I. Affleck and A. W. W. Ludwig, “Exact conformal-field-theory results on the multichannel Kondo effect: Single-fermion Green’s function, self-energy, and resistivity,” *Phys. Rev. B* **48**, 7297 (1993).
- [46] A. W. W. Ludwig and I. Affleck, “Exact conformal-field-theory results on the multi-channel Kondo effect: Asymptotic three-dimensional space- and time-dependent multi-point and many-particle Green’s functions,” *Nucl. Phys. B* **428**, 545 (1994).
- [47] K. M. Stadler, Ph.D. thesis, Ludwig-Maximilians-Universität München (2019).
- [48] J. Ye, “Solution of the two-channel spin-flavor Kondo model,” *Phys. Rev. B* **56**, R489 (1997).
- [49] Y. Wang, E. Walter, S.-S. B. Lee, K. M. Stadler, J. von Delft, A. Weichselbaum, and G. Kotliar, “Global phase diagram of a spin-orbital Kondo impurity model and the suppression of Fermi-liquid scale,” *Phys. Rev. Lett.* **124**, 136406 (2020).
- [50] A. Weichselbaum, “Non-abelian symmetries in tensor networks: A quantum symmetry space approach,” *Ann. Phys.* **327**, 2972 (2012).
- [51] A. Weichselbaum, “Tensor networks and the numerical renormalization group,” *Phys. Rev. B* **86**, 245124 (2012).
- [52] A. Weichselbaum and J. von Delft, “Sum-rule conserving spectral functions from the numerical renormalization group,” *Phys. Rev. Lett.* **99**, 076402 (2007).
- [53] S.-S. B. Lee and A. Weichselbaum, “Adaptive broadening to improve spectral resolution in the numerical renormalization group,” *Phys. Rev. B* **94**, 235127 (2016).
- [54] See Supplemental Material for tables presenting detailed fusion rules and contributions to low-energy spectra, which contains Refs. [55, 56].
- [55] C. J. Cummins, “su(n) and sp($2n$) WZW fusion rules,” *J. Phys. A: Math. Gen.* **24**, 391 (1991).
- [56] P. Di Francesco, P. Mathieu, and D. Sénéchal, *Conformal Field Theory* (Springer, 1997).
- [57] J. von Delft, Ph.D. thesis, Cornell University (1995).
- [58] A. W. W. Ludwig, “Field theory approach to critical quantum impurity problems and applications to the multichannel Kondo effect,” *Int. J. Mod. Phys. B* **8**, 347 (1994).
- [59] J. L. Cardy, “Conformal invariance and surface critical behavior,” *Nuclear Physics B* **240**, 514 (1984).
- [60] The quantum numbers of $\tilde{\Psi}_{\text{orb}}$ differ from those of Φ_{orb} (and hence also of \mathbf{T} , \mathbf{J}_{orb}), since the same is true for their parent states, reflecting the fact that the latter undergo a true level crossing. Ditto for $\tilde{\Psi}_{\text{sp}}$ vs. Φ_{sp} (and \mathbf{S} , \mathbf{J}_{sp}). In contrast to $\mathbf{S} \cdot \Phi_{\text{sp}}$, it is hence not possible to couple \mathbf{S} and $\tilde{\Psi}_{\text{sp}}$ to a spin singlet, needed for computing $\chi_{\text{sp}}^{\text{imp,bath}}$. Instead, we speculate that the role of $(\int dt' S^a \Phi_{\text{sp}}^a)^2$ could be taken, e.g., by $\int dt' S^a (\tilde{\Psi}_{\text{sp}}^\dagger)_\sigma \int dt'' S^a (\tilde{\Psi}_{\text{sp}})_\sigma$.
- [61] I. Affleck, “Conformal field theory approach to the Kondo effect,” *Acta Phys. Polon. B* **26**, 1869 (1995).
- [62] J. Fuchs and C. Schweigert, *Symmetries, Lie Algebras and Representations: A Graduate Course for Physicists* (Cambridge University Press, 1997) p.335, Eq. (19.14).
- [63] T. A. Costi, “Kondo effect in a magnetic field and the magnetoresistivity of Kondo alloys,” *Phys. Rev. Lett.* **85**, 1504 (2000).
- [64] A. A. Khajetoorians, M. Valentyuk, M. Steinbrecher, T. Schlenk, A. Shick, J. Kolorenc, A. I. Lichtenstein, T. O. Wehling, R. Wiesendanger, and J. Wiebe, “Tuning emergent magnetism in a Hund’s impurity,” *Nat. Nanotechnol.* **10**, 958 (2015).
- [65] A. Horvat, R. Žitko, and J. Mravlje, “Non-Fermi-liquid fixed point in multi-orbital Kondo impurity model relevant for Hund’s metals,” [arXiv:1907.07100 \[cond-mat.str-el\]](https://arxiv.org/abs/1907.07100) (2019).

Supplemental Material for “Uncovering Non-Fermi-Liquid Behavior in Hund Metals: Conformal Field Theory Analysis of an $SU(2) \times SU(3)$ Spin-Orbital Kondo Model”

E. Walter, K. M. Stadler, S.-S. B. Lee, Y. Wang, G. Kotliar, A. Weichselbaum, and J. von Delft

Citations and equation numbers refer to references and equations given in the main text.

Below we provide a number of tables needed for various non-Abelian bosonization and Kac-Moody fusion schemes used in the main text: $U(1) \times SU(2)_3 \times SU(3)_2$, $U(1) \times SU(6)_1$, $U(1) \times SU(2)_2 \times SU(2)_2$, and $U(1) \times SU(4)_1$.

The fusion rules for the $SU(N)_k$ Kac-Moody (KM) algebra differ from those of the $SU(N)$ Lie algebra in that some Young diagrams arising for the latter are forbidden for the former (such as Young diagrams with more than k columns, reflecting the fact that only two distinct spin species are available when constructing $SU(N)_k$ representations). However, note that these fusion rules are in general more complicated than simply crossing out diagrams with more than k columns. For example, in Table S3 for $SU(2)_3$, not all representations with $S'' \leq 3/2$ are allowed. We constructed the KM fusion tables given below using a general recipe due to Cummins [55], explained in pedagogical detail in Sec. 16.2.4 of [56].

$U(1) \times SU(2)_3 \times SU(3)_2$

Table S1. The few lowest values of the quantum numbers q , S and $\lambda = (\lambda_1, \lambda_2)$ labeling $U(1)$ charge, $SU(2)_3$ spin and $SU(3)_2$ orbital multiplets, their contributions to the energies $E(q, S, \lambda)$ of Eq. (12a), and the dimensions d of the spin and orbital multiplets. $\kappa_2(S)$, $\kappa_3(\lambda)$ are given in Eqs. (12b), (12c).

q	0	± 1	± 2	± 3	± 4	± 5
$\frac{1}{12}q^2$	0	$\frac{1}{12}$	$\frac{1}{3}$	$\frac{3}{4}$	$\frac{4}{3}$	$\frac{25}{12}$
S	0	$\frac{1}{2}$	1	$\frac{3}{2}$	2	$\frac{5}{2}$
$\frac{1}{5}\kappa_2(S)$	0	$\frac{3}{20}$	$\frac{2}{5}$	$\frac{3}{4}$	$\frac{6}{5}$	$\frac{7}{4}$
$d(S)$	1	2	3	4	5	6
(λ_1, λ_2)	(0,0)	(1,0)	(0,1)	(2,0)	(0,2)	(1,1)
λ	\bullet	\square	$\begin{array}{ c } \hline \square \\ \hline \end{array}$	$\begin{array}{ c c } \hline \square & \square \\ \hline \end{array}$	$\begin{array}{ c c } \hline \square & \square \\ \hline \end{array}$	$\begin{array}{ c c } \hline \square & \square \\ \hline \end{array}$
$\frac{1}{5}\kappa_3(\lambda)$	0	$\frac{4}{15}$	$\frac{4}{15}$	$\frac{2}{3}$	$\frac{2}{3}$	$\frac{3}{5}$
$d(\lambda)$	1	3	3	6	6	8

Table S2. $SU(3)_2$ fusion rules, listing various direct product decompositions of the form $\lambda \otimes \lambda' = \sum_{\oplus} \lambda''$. Crossed-out diagrams denote additional irreps occurring when considering direct product decompositions for $SU(3)$ instead of $SU(3)_2$.

$d(\lambda)$	$\kappa_3(\lambda)$	(λ_1, λ_2)	λ	λ'	\square	$\begin{array}{ c } \hline \square \\ \hline \end{array}$
3	$\frac{4}{3}$	(1,0)	\square	\square	$\square \oplus \square$	$\bullet \oplus \begin{array}{ c } \hline \square \\ \hline \end{array}$
3	$\frac{4}{3}$	(0,1)	$\begin{array}{ c } \hline \square \\ \hline \end{array}$	$\begin{array}{ c } \hline \square \\ \hline \end{array}$	$\bullet \oplus \begin{array}{ c } \hline \square \\ \hline \end{array}$	$\square \oplus \begin{array}{ c } \hline \square \\ \hline \end{array}$
6	$\frac{10}{3}$	(2,0)	$\begin{array}{ c c } \hline \square & \square \\ \hline \end{array}$	$\begin{array}{ c c } \hline \square & \square \\ \hline \end{array}$	$\begin{array}{ c c } \hline \square & \square \\ \hline \end{array} \oplus \begin{array}{ c c } \hline \square & \square \\ \hline \end{array}$	$\square \oplus \begin{array}{ c } \hline \square \\ \hline \end{array}$
6	$\frac{10}{3}$	(0,2)	$\begin{array}{ c c } \hline \square & \square \\ \hline \end{array}$	$\begin{array}{ c c } \hline \square & \square \\ \hline \end{array}$	$\begin{array}{ c c } \hline \square & \square \\ \hline \end{array} \oplus \begin{array}{ c c } \hline \square & \square \\ \hline \end{array}$	$\begin{array}{ c c } \hline \square & \square \\ \hline \end{array} \oplus \begin{array}{ c c } \hline \square & \square \\ \hline \end{array}$
8	3	(1,1)	$\begin{array}{ c c } \hline \square & \square \\ \hline \end{array}$	$\begin{array}{ c c } \hline \square & \square \\ \hline \end{array}$	$\square \oplus \begin{array}{ c } \hline \square \\ \hline \end{array}$	$\begin{array}{ c } \hline \square \\ \hline \end{array} \oplus \square$

Table S3. $SU(2)_3$ fusion rules, listing various direct product decompositions of the form $S \otimes S' = \sum_{\oplus} S''$. Crossed-out numbers denote additional irreps occurring when considering direct product decompositions for $SU(2)$ instead of $SU(2)_3$.

$d(S)$	$\kappa_2(S)$	S	S'	$\frac{3}{2}$
1	0	0	0	$\frac{3}{2}$
2	$\frac{3}{4}$	$\frac{1}{2}$	$\frac{1}{2}$	$1 \oplus \cancel{2}$
3	2	1	1	$\frac{1}{2} \oplus \cancel{\frac{3}{2}} \oplus \cancel{\frac{5}{2}}$
4	$\frac{15}{4}$	$\frac{3}{2}$	$\frac{3}{2}$	$0 \oplus \cancel{1} \oplus \cancel{2} \oplus \cancel{3}$

U(1)×SU(6)₁

Table S4. The few lowest values of the quantum numbers q and $\lambda = (\lambda_1, \lambda_2, \lambda_3, \lambda_4, \lambda_5)$, labeling U(1) charge and SU(6)₁ flavor multiplets, their contributions to the eigenenergies $E(q, \lambda)$ of Eq. (22a), and the dimensions d of the flavor multiplets. Single-column Young diagrams with i boxes have $\lambda_j = \delta_{ij}$. $\kappa_6(\lambda)$ is given in Eq. (22b).

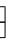










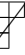

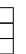
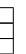


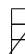
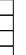
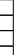


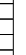
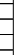

q	0	± 1	± 2	± 3	± 4	± 5
$\frac{1}{12}q^2$	0	$\frac{1}{12}$	$\frac{1}{3}$	$\frac{3}{4}$	$\frac{4}{3}$	$\frac{25}{12}$
λ	•	□				
$\frac{1}{7}\kappa_6(\lambda)$	0	$\frac{5}{12}$	$\frac{2}{3}$	$\frac{3}{4}$	$\frac{2}{3}$	$\frac{5}{12}$
$d(\lambda)$	1	6	15	20	15	6

Table S5. SU(6)₁ fusion rules, listing some direct product decompositions $\lambda \otimes \lambda' = \sum_{\oplus} \lambda''$, with $\lambda' = \square$. Crossed-out diagrams denote additional irreps occurring when considering direct product decompositions for SU(6) instead of SU(6)₁.

$d(\lambda)$	$\kappa_6(\lambda)$	$(\lambda_1, \lambda_2, \lambda_3, \lambda_4, \lambda_5)$	λ	λ'	
1	0	(0,0,0,0,0)	•	•	
6	$\frac{35}{12}$	(1,0,0,0,0)	□	□	 ⊕ 
15	$\frac{14}{3}$	(0,1,0,0,0)			 ⊕  ⊕ 
20	$\frac{21}{4}$	(0,0,1,0,0)			 ⊕  ⊕ 
15	$\frac{14}{3}$	(0,0,0,1,0)			• ⊕  ⊕ 
6	$\frac{35}{12}$	(0,0,0,0,1)			□ ⊕ 

U(1)×SU(2)₂×SU(2)₂

Table S6. The few lowest values of the quantum numbers q , S and λ , labeling U(1) charge, SU(2)₂ spin and SU(2)₂ orbital multiplets, respectively, their contributions to the eigenenergies $E(q, S, \lambda)$ of Eq. (A1a), and the dimensions d of the spin and flavor multiplets. $\kappa_2(S)$ and $\kappa_2(\lambda)$ are given in Eq. (A1b).

q	0	± 1	± 2	± 3
$\frac{1}{8}q^2$	0	$\frac{1}{8}$	$\frac{1}{2}$	$\frac{9}{8}$
S, λ	0	$\frac{1}{2}$	1	$\frac{3}{2}$
$\frac{1}{4}\kappa_2(S), \frac{1}{4}\kappa_2(\lambda)$	0	$\frac{3}{16}$	$\frac{1}{2}$	$\frac{15}{16}$
$d(S), d(\lambda)$	1	2	3	4

Table S7. SU(2)₂ fusion rules, listing various direct product decompositions of the form $S \otimes S' = \sum_{\oplus} S''$. Crossed-out numbers denote additional irreps occurring when considering direct product decompositions for SU(2) instead of SU(2)₂.

$d(S)$	$\kappa_2(S)$	S	S'	$\frac{1}{2}$
1	0	0	0	$\frac{1}{2}$
2	$\frac{3}{4}$	$\frac{1}{2}$	$\frac{1}{2}$	0 ⊕ 1
3	2	1	1	$\frac{1}{2} \oplus \frac{3}{2}$

$U(1) \times SU(4)_1$

Table S8. The few lowest values of the quantum numbers q and $\lambda = (\lambda_1, \lambda_2, \lambda_3)$, labeling $U(1)$ charge and $SU(4)_1$ flavor multiplets, their contributions to the eigenenergies $E(q, \lambda)$ of Eq. (A2a), and the dimensions d of the flavor multiplets. $\kappa_4(\lambda)$ is given in Eq. (A2b).

q	0	± 1	± 2	± 3
$\frac{1}{8}q^2$	0	$\frac{1}{8}$	$\frac{1}{2}$	$\frac{9}{8}$
$(\lambda_1, \lambda_2, \lambda_3)$	(0,0,0)	(1,0,0)	(0,1,0)	(0,0,1)
λ	•	□	▢	▣
$\frac{1}{5}\kappa_4(\lambda)$	0	$\frac{3}{8}$	$\frac{1}{2}$	$\frac{3}{8}$
$d(\lambda)$	1	4	6	4

Table S9. $SU(4)_1$ fusion rules, listing some direct product decompositions $\lambda \otimes \lambda' = \sum_{\oplus} \lambda''$, with $\lambda' = \square$. Crossed-out diagrams denote additional irreps occurring when considering direct product decompositions for $SU(4)$ instead of $SU(4)_1$.

$d(\lambda)$	$\kappa_4(\lambda)$	$(\lambda_1, \lambda_2, \lambda_3)$	λ	λ'	
1	0	(0,0,0)	•	□	□
4	$\frac{15}{8}$	(1,0,0)	□	□	▢ ⊕ ▣
6	$\frac{5}{2}$	(0,1,0)	▢	□	▣ ⊕ ▢
4	$\frac{15}{8}$	(0,0,1)	▣	□	• ⊕ ▢